
Figures and figure supplements

Distinct roles for two *Caenorhabditis elegans* acid-sensing ion channels in an ultradian clock

Eva Kaulich et al

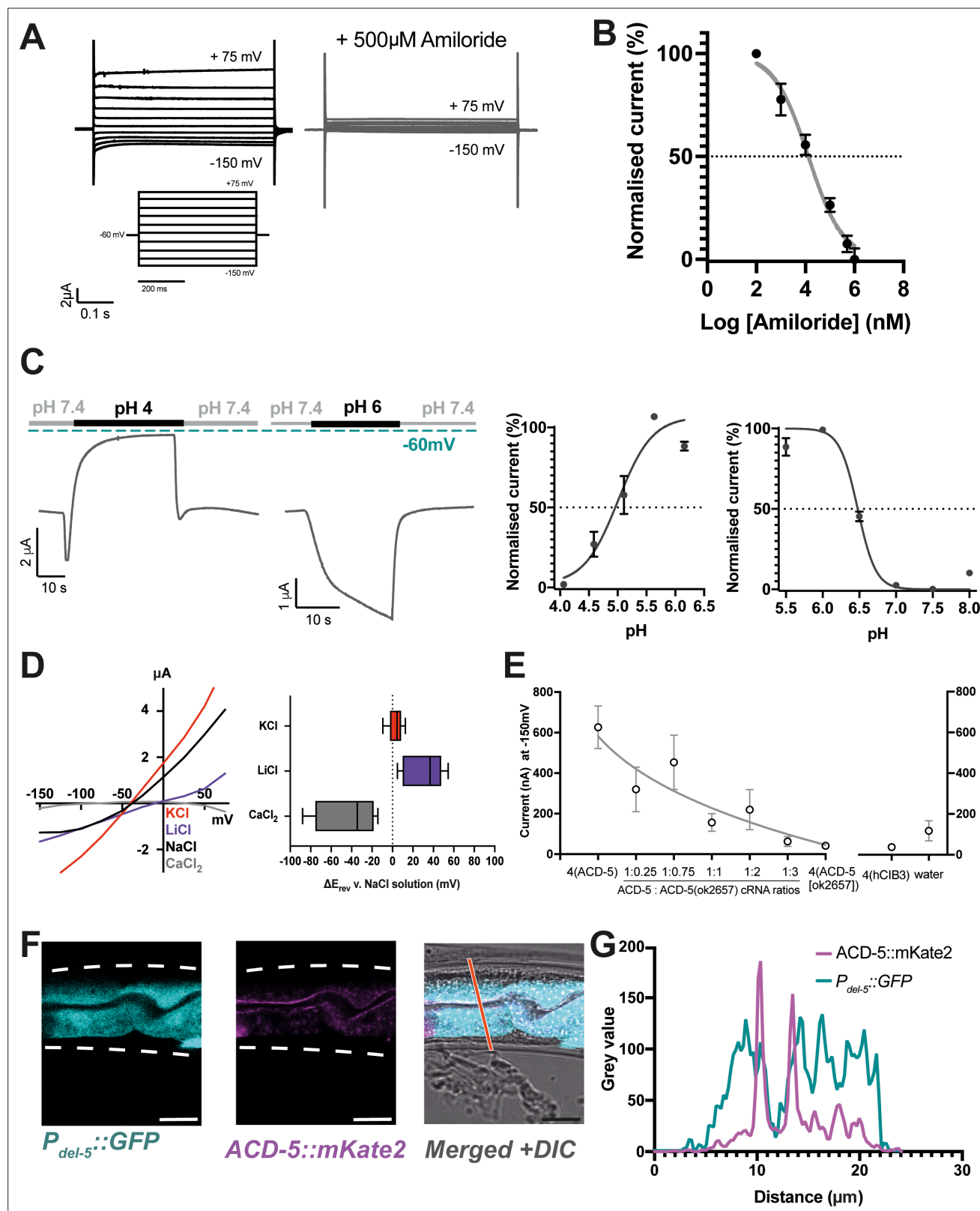


Figure 1. ACD-5 is an amiloride-sensitive, acid-sensing cation channel on the luminal membrane of the intestine. (A) ACD-5 currents are amiloride-sensitive. Representative ACD-5 transients in *Xenopus* oocytes in the presence and absence of amiloride and (B) normalised amiloride-dose response curve (I/I_{max} as percentage) for ACD-5, showing a half-maximal inhibitory concentration (IC_{50}) of 131 μ M ($LogIC_{50}=4.118$) ($N=8$) indicated by the dashed line (curve fitted as described below). Error bars represent mean \pm SEM. (C) ACD-5 can form a homomeric acid-sensing ion channel. Left panel:

Figure 1 continued on next page

Figure 1 continued

Representative trace of ACD-5-expressing *Xenopus* oocytes subjected to a down-step to pH 4 or 6. Currents were recorded at a holding potential of -60mV and traces are baseline-subtracted and drift-corrected using the Roboocyte2+ (Multichannels) software. Right panel: pH-dose dependence (I/I_{max} expressed as percentage). ACD-5-expressing oocytes were perfused with solutions of decreasing pH from pH 6 (left), showing an inhibitory pH_{50} of 4.90 ($N=5$); when perfused with increasing pH from pH 6 (right), showing an excitatory pH_{50} of 6.48 ($N=7$). Currents were recorded at a holding potential of -60mV , normalised to maximal currents and best fitted with the Hill's equation (Nonlin fit Log(inhibitor) versus normalised response – variable slope) in GraphPad Prism. Error bars represent mean \pm SEM. **(D)** Current-voltage (IV) curve (left) and change in reversal potential, ΔE_{rev} when shifting from a NaCl solution to CaCl_2 , KCl, or LiCl (right). $N=12$ oocytes. Presented as median and IQR (Tukey method). **(E)** ACD-5(ok2657) is a dominant mutation. Expression of varying ratios of ACD-5(ok2657) with a constant concentration of wild-type ACD-5 in *Xenopus* oocytes. hCIB3 (Calcium and integrin-binding family member 3) was used as a filler to account for amount of cRNA injected. Mean \pm SEM. $9 < N < 19$ for each ratio. **(F)** ACD-5 is localised at the apical (luminal) intestinal membrane. Localisation of mKate2-C-terminally tagged ACD-5 (*ljlEx1470* (*Pacd-5::acd-5(no stop) cDNA::mKate2*)) shows apical membrane localisation (magenta). Cytoplasm of the intestinal cells is shown in cyan (*ljlEx1349* (*Pdel-5::GFP*)). **(G)** Intensity profile taken at the part of the intestine indicated by the red line. Scale bar: $10\mu\text{m}$.

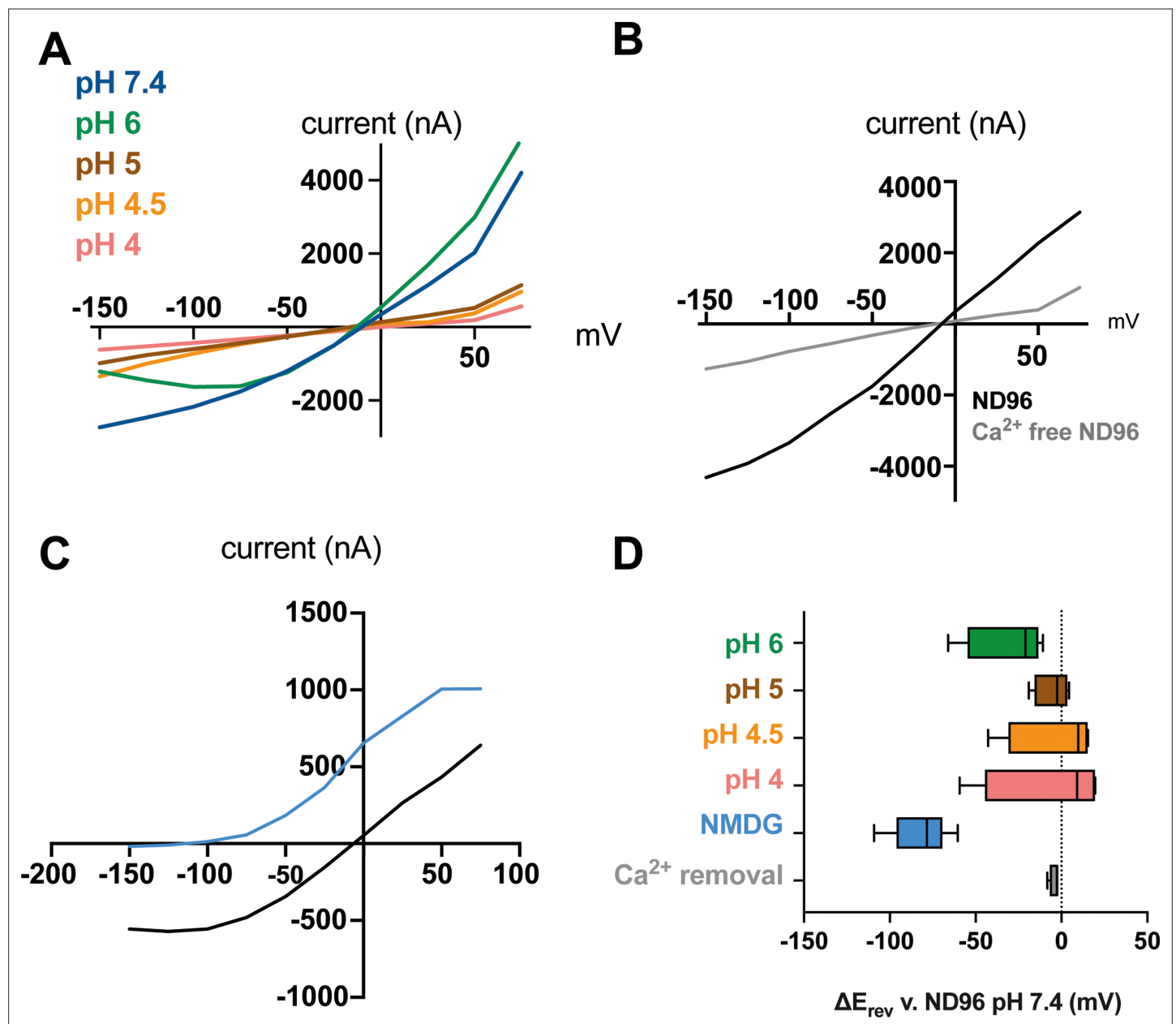


Figure 1—figure supplement 1. Further characterisation of ACD-5 homomeric channel properties. (A) Representative current-voltage (I-V) relationships perfusing different pH solution over the oocyte. (B) Representative current-voltage relationships after removal of Ca²⁺ from the solution. (C) Representative current-voltage relationships in a basal solution (ND96, pH 7.4) and after removal of Na⁺ from the solution (NMDG, pH 7.4). (D) Summary of reversal potential E_{rev} of data presented in (A–C). Dashed line represents the E_{rev} for the Na⁺ solution. N (top to bottom)=4, 4, 4, 4, 8, 4. Data are presented as boxplots with median and IQD (interquartile distance, as calculated by the Tukey method).

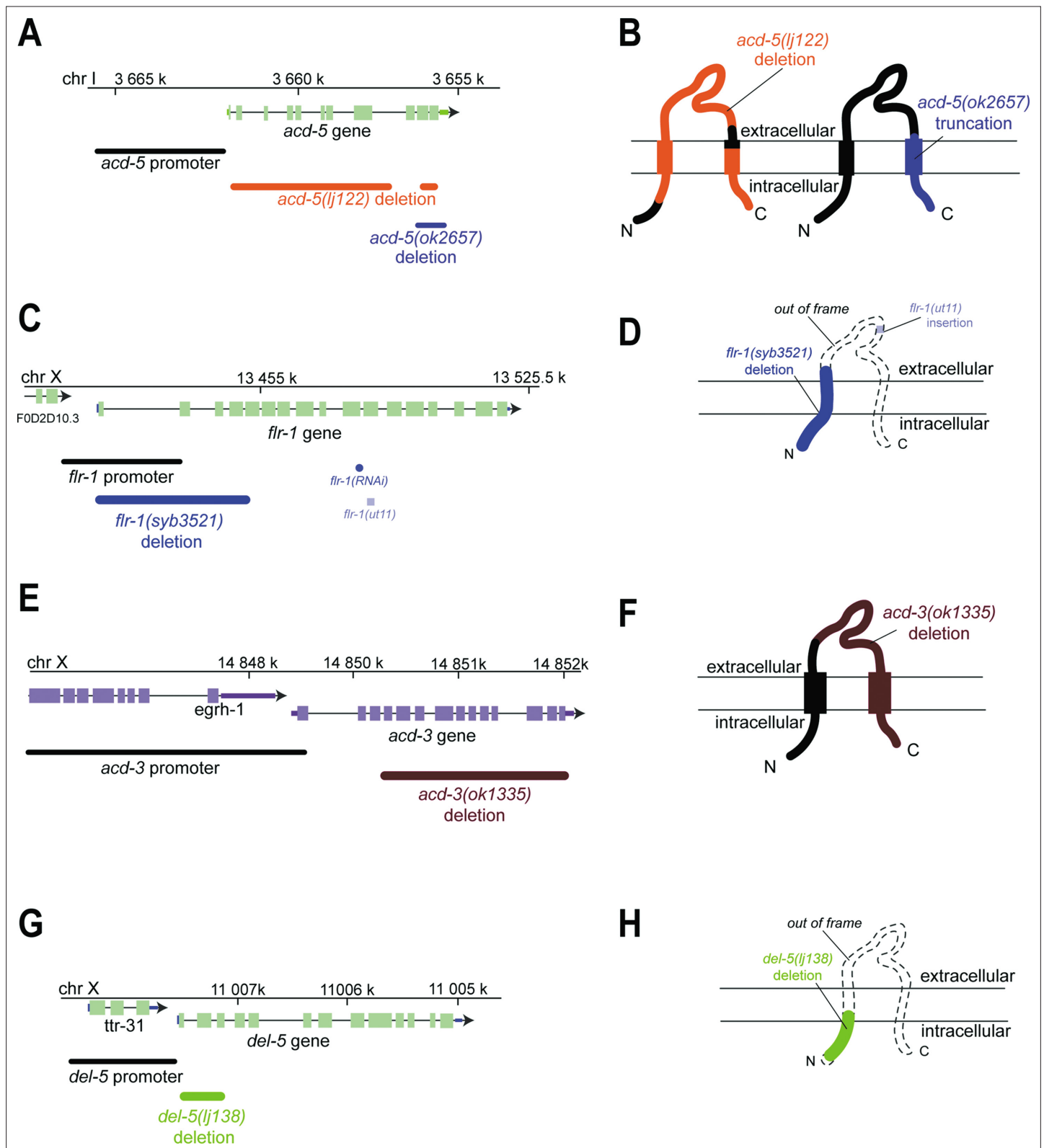


Figure 1—figure supplement 2. Genomic regions and schematic of predicted protein structures of the intestinal DEG/ENaCs, showing mutations used in this study. **(A, C, E, G)** Genomic region for the genes indicated. Boxes indicate exons, lines indicate introns, and chr indicates chromosome. Endogenous promoter region used, mutations and RNAi used in this study are shown. **(B, D, F, H)** Schematic of predicted protein structure with two transmembrane helices, and cytosolic N- and C-terminus and an extracellular domain, typical of DEG/ENaC subunits. Mutations used in the study are indicated for each gene and protein. Black indicates intact; coloured indicates deleted; dashed line indicates out of frame.

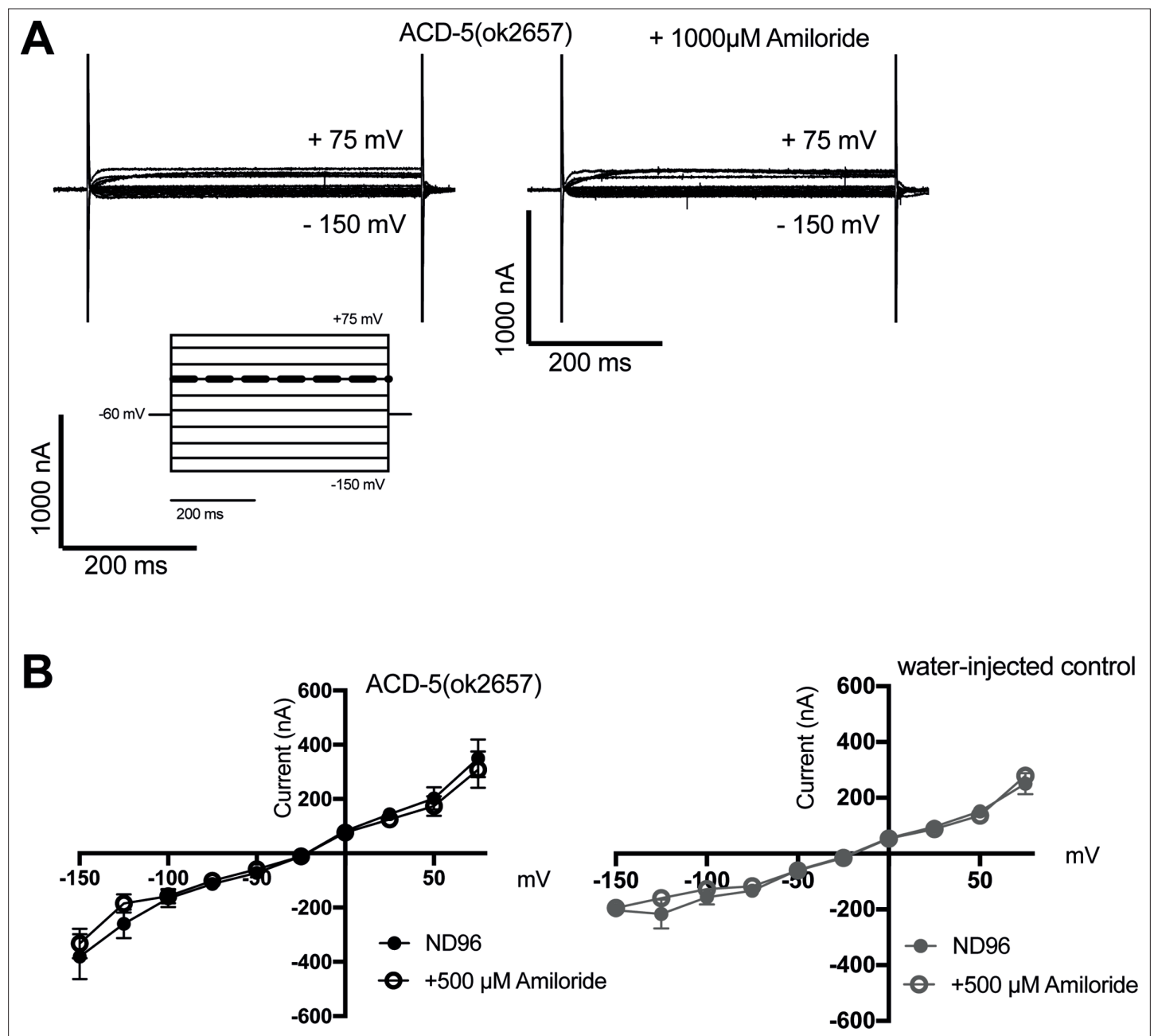


Figure 1—figure supplement 3. Characterisation of ACD-5 channels carrying the *ok2657* mutation in *Xenopus* oocytes. **(A)** Representative transients and **(B)** current-voltage (I-V) relationships of *Xenopus* oocytes injected with *acd-5(ok2657)* cRNA in the presence and absence of amiloride, and a water-injected control. N=10. Error bars represent mean and SEM.

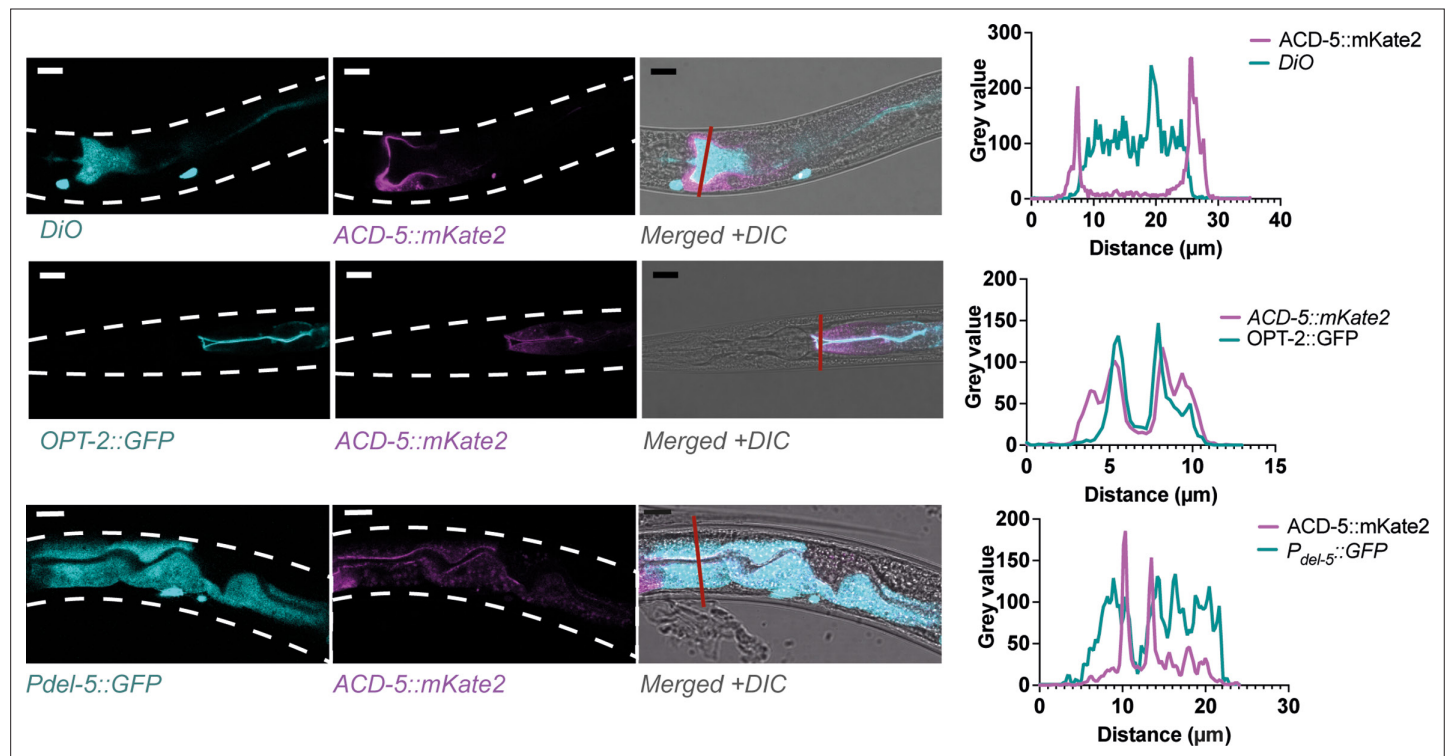


Figure 1—figure supplement 4. ACD-5 localises to the apical membrane. Co-localisation of ACD-5::mKate2 (*ljEx1470*) with luminal DiO fluorescence, an apical membrane marker *ryEx133* [*pKN114* (*opt-2p::opt-2(aa1-412)::GFP*)] and a cytoplasmic marker *ljEx1349* (*Pdel-5::GFP*) with intensity profiles. Scale bar: 10 μm.

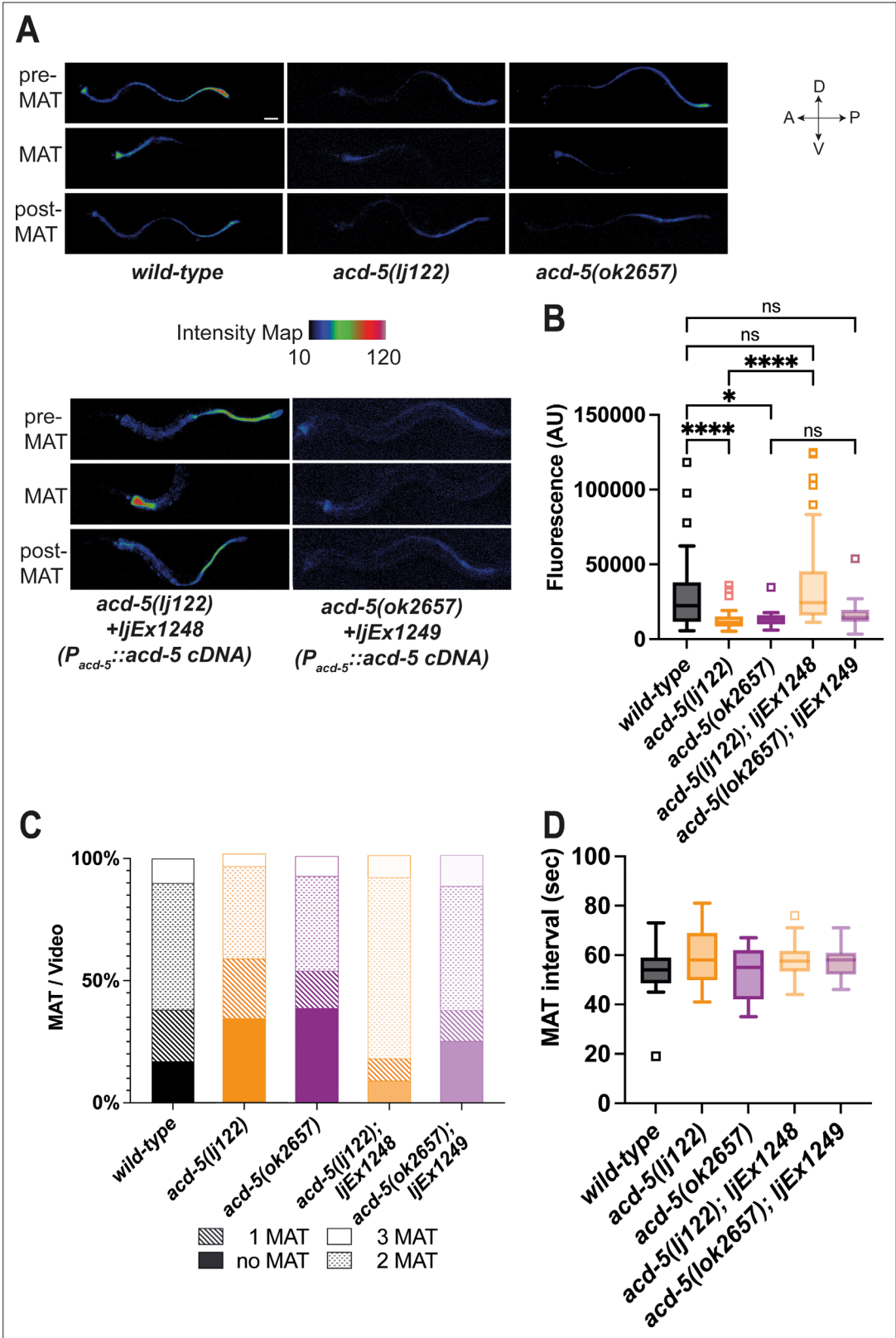


Figure 2. ACD-5 mutations show disruptions in intestinal lumen acidity and luminal proton oscillations. (A) ACD-5 is important to establish and maintain an acidic intestinal pH. Heat map of pixel fluorescence intensity with red representing highest intensity (high acidity), and black lowest intensity (low acidity), after feeding on the pH-sensitive probe Kansas Red (KR35) for 30min (10μM). Maximum anterior transition (MAT)±15s (pre/post-MAT)

Figure 2 continued on next page

Figure 2 continued

during the DMP extracted from videos of free-moving animals are shown. Rescue lines express the *ljEx1248(Pacd-5::acd-5 cDNA)* or *ljEx1249(Pacd-5::acd-5 cDNA)* extrachromosomal array, respectively. D=dorsal, V=ventral, A=anterior, P=posterior. Scale bar: 50µm. **(B)** *acd-5(lj122)* mutants (**** $p<0.0001$) and *acd-5(ok2657)* mutants (* $p=0.0309$) display lower intestinal lumen pH compared to the wild-type. This could be rescued only in the *acd-5(lj122)* mutants (**** $p<0.0001$). Quantification of fluorescence in the MAT. Data are presented as median and IQR (Tukey method, N=24, 19, 9, 20, and 12, respectively). Outliers are indicated by squared boxes. Kruskal-Wallis test with Dunn's multiple comparison test. **(C)** *acd-5* mutants display a reduced number of MATs. Quantification of MATs per 2-min video recording shown as percentages of animals displaying 1, 2 or 3 MATs. Median and IQR (Tukey method, N=29, 38, 13, 23, and 16, respectively). **(D)** MAT intervals are not affected by *acd-5* mutations. Time interval of MAT of *acd-5* mutants, wild-type and rescues. Kruskal-Wallis test with Dunn's multiple comparison test was non-significant ($P=0.405$). Data are presented as median and IQR (Tukey method). N=21, 18, 7, 20, and 12, respectively.

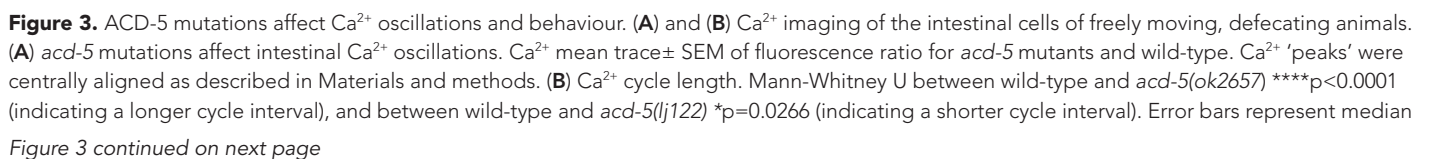


Figure 3 continued

and IQR, N=50, 55, and 53, respectively (i.e., individual intervals from 15 animals for each genotype, recorded for 5min each). **(C)** ACD-5(ok2657) is a dominant mutation. Comparison of defecation cycle length in *acd-5* mutant and overexpression strains. Kruskal-Wallis test and post hoc Dunnett's multiple comparisons test found no significant difference between wild-type and *acd-5(lj122)* animals ($p>0.9999$) but a significant difference from wild-type for homo- and heterozygous *acd-5(ok2657)* animals and wild-type animals expressing *lJEx1500(Pacd-5::acd-5(ok2657))* or *lJEx1507(Pges-1::acd-5(ok2657))* ($****p<0.0001$); those overexpressing wild-type *lJEx1248(Pacd-5::acd-5cDNA)* were not significantly different from wild-type ($p>0.9999$). Median and IQR. $50<N<75$ (10–15 animals for each group, five cycles for each animal). **(D)** and **(E)** Effect of *acd-5* alleles on the defecation interval of *itr-1(sa73)* animals. **(D)** DMP interval length (median and IQR). Kruskal-Wallis test was significant ($****p<0.0001$). A post hoc Dunn's multiple comparison test indicated that compared to the wild-type, *acd-5(ok2657)* mutants and the *itr-1* single and double mutants ($****p<0.0001$) all showed a significant increase in interval length. **(E)** Coefficient of variation in cycle length. *acd-5(lj122)* ($**p=0.001$) or the *acd-5(ok2657)* ($****p<0.0001$) double mutants showed significant increase in variability, similar to the *itr-1* single mutants. Error bars represent median and IQR. $75<N<130$ (15–26 animals \times 5 cycles for each). See also **Figure 3—figure supplement 4**, showing comparison of cumulative distribution of cycle length and CV. **(F)** Effect of *acd-5* alleles on defecation cycle length of *pbo-4(ok538)* animals. DMP interval length (median and IQR). The Kruskal-Wallis test was significant with a post hoc Dunn's multiple comparison test indicating that only *acd-5(ok2657)* mutants had increased cycle length ($****p<0.0001$); *pbo-4* single ($p=0.885$) and double mutants (both $p=1$) were not significantly different from wild-type. *pbo-4(ok538)* significantly reduced the cycle length of *acd-5(ok2657)* animals ($****p<0.0001$). Error bars represent median and IQR. N=60 (12 animals \times 5 cycles, wild-type), 40 (8 \times 5 cycles, all other strains). **(G)** Schematic of the relationship between ACD-5, proton release and Ca^{2+} oscillations. Release of protons at the luminal membrane via NHX channels (which could include PBO-4) and/or V-ATPase (of which VHA-6 is a component) results in decrease in luminal pH which inhibits the ACD-5 channel. Proton oscillations (curved line) from pH 4 to 6 activate the ACD-5 channel at pH 6 which in turn influences (but does not drive) *itr-1*-mediated Ca^{2+} oscillations.

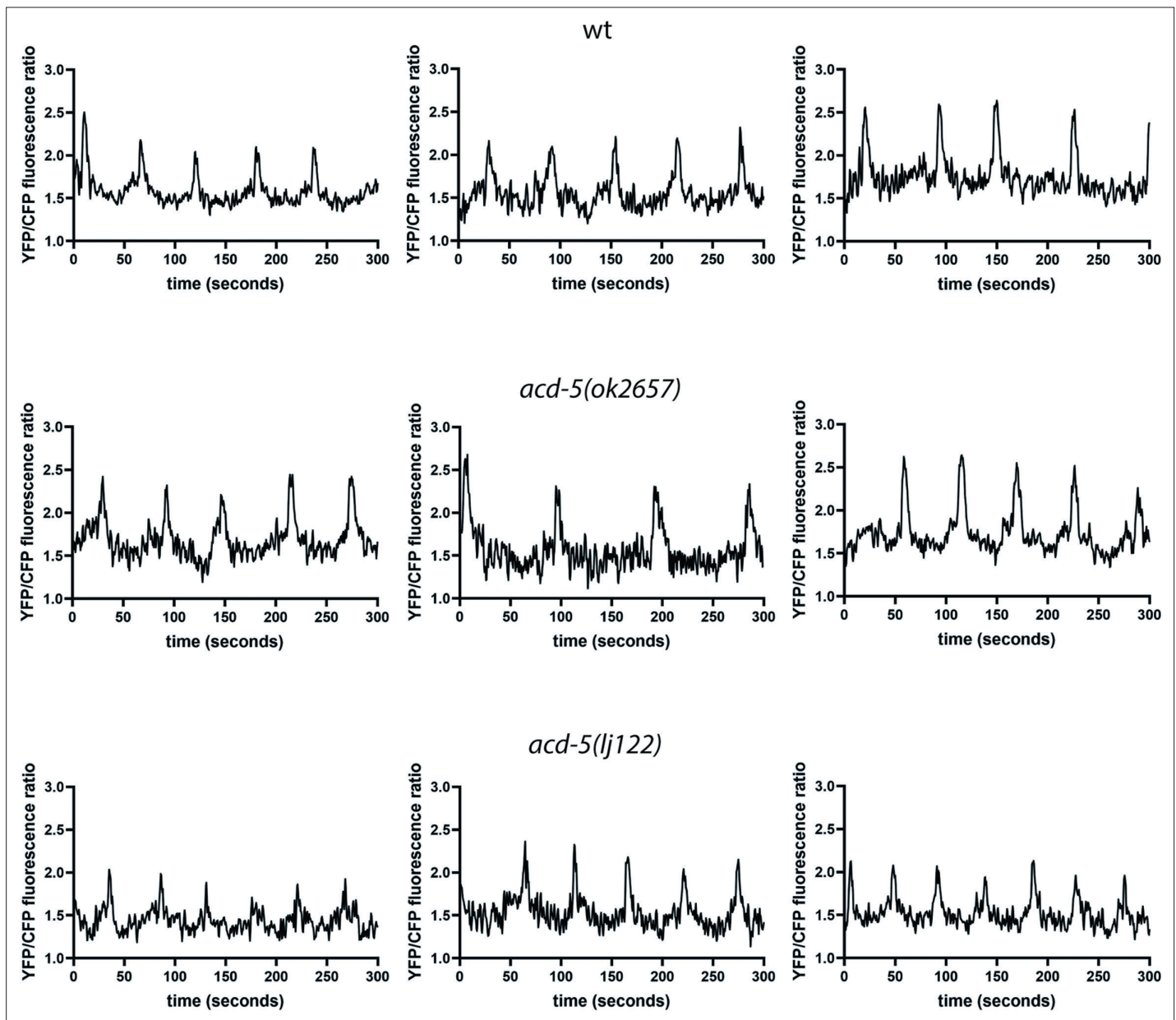


Figure 3—figure supplement 1. ACD-5 modifies intestinal Ca^{2+} oscillations. Ca^{2+} imaging of the posterior intestinal (int9) cells of freely moving, defecating animals. Three representative example traces of intestinal Ca^{2+} transients of the wild-type, *acd-5(ok2657)*, and *acd-5(lj122)* mutants over a 5-min time period.

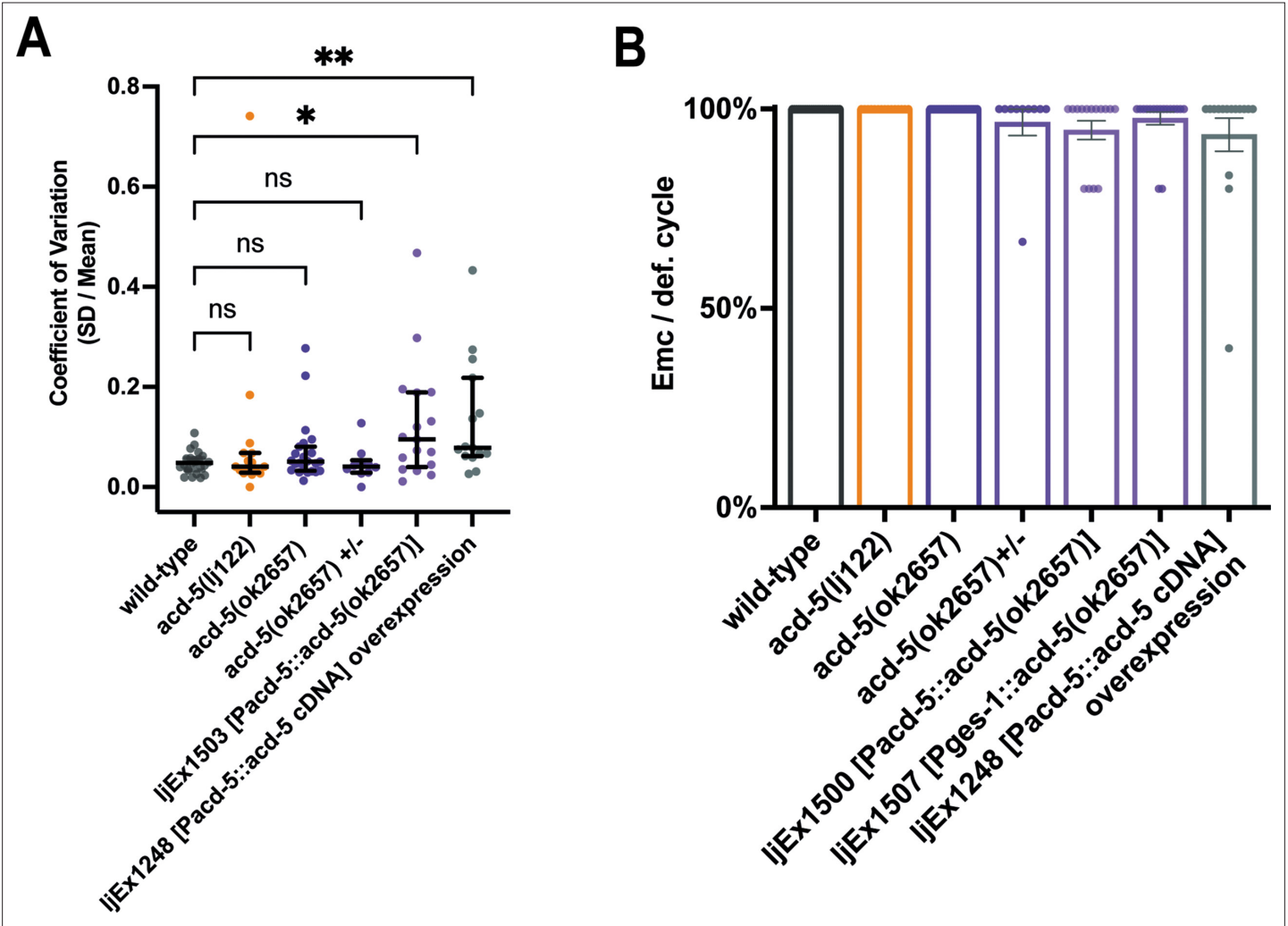


Figure 3—figure supplement 2. Effect of *acd-5(ok2657)* overexpression on variation of defecation interval length and DMP. **(A)** Variability between DMP cycles. Error bars represent median and IQR. Significance was assessed by a Kruskal-Wallis test with Dunn's multiple comparison test (*p=0.0466; **p=0.0093). N>10 animals × 5 cycles per animal. **(B)** Quantification of EMCs. Significance was assessed by a Kruskal-Wallis test with Dunn's multiple comparison test which was not statistically significant. Left to right, comparing with wt, p=1, 1, 1, 0.1910, 1, and 0.6449; *acd-5(ok2657)* versus *acd-5(ok2657) ±p=1*; *acd-5(ok2657)* versus *lJEx1500* p=0.1326; *acd-5(ok2657)* versus *lJEx1507* p=1; *acd-5(ok2657)* versus *lJEx1248* p=0.5110. Error bars represent mean and SEM. N>10 animals, five cycles each animal. EMC, enteric muscle contraction.

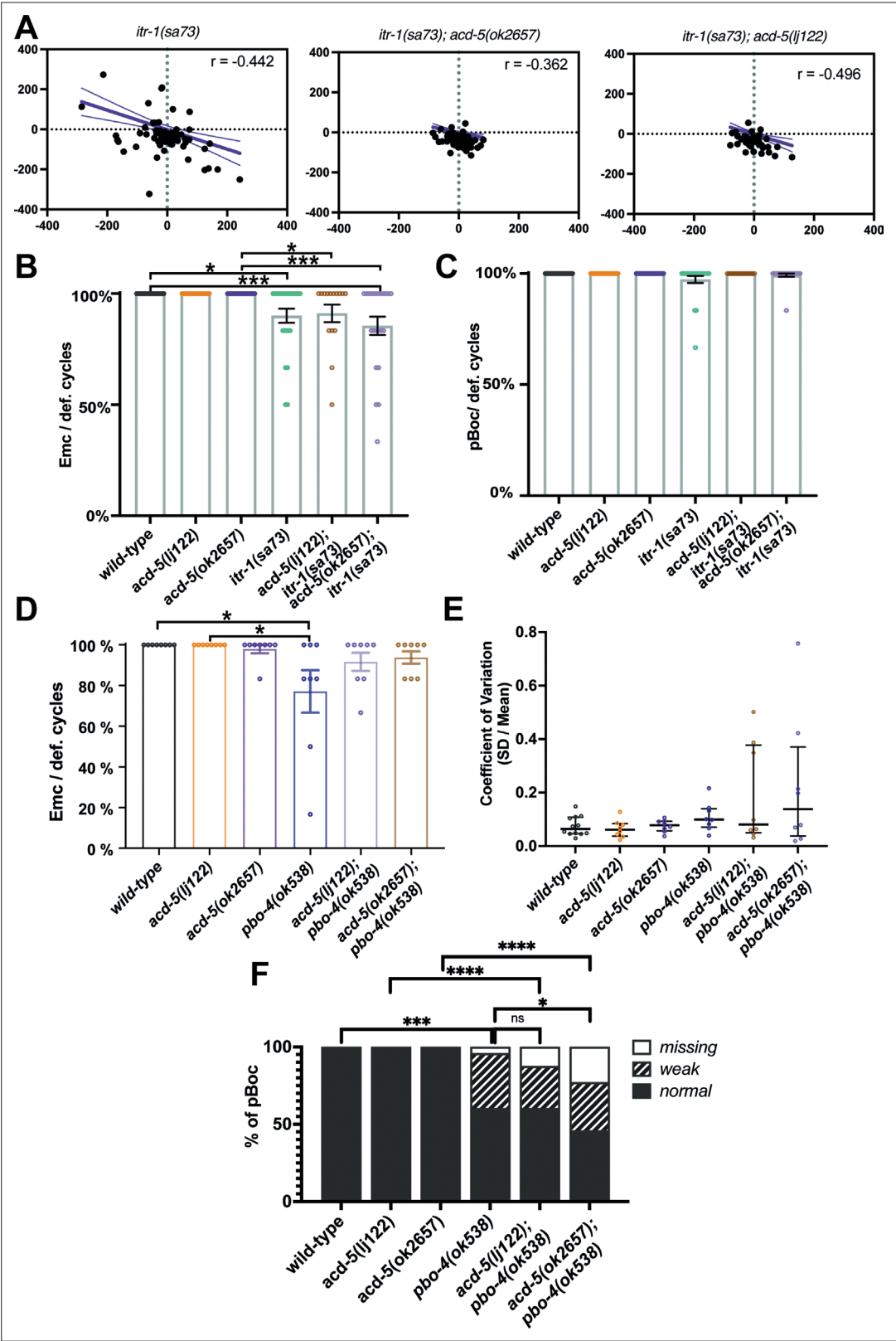


Figure 3—figure supplement 3. *acd-5* alleles alter the defecation phenotype of *itr-1* and *pbo-4* loss of function animals. (A) Analysis of the defecation cycle in *itr-1(sa73)* single and double mutants with *acd-5* reveals compensatory behaviour in the oscillator. Scatter plot of the change in interval duration in one cycle pair compared to the subsequent cycle pair, for *itr-1(sa73)* mutants. T(n) is the period of the cycle n. Linear regression (Pearson's

Figure 3—figure supplement 3 continued on next page

Figure 3—figure supplement 3 continued

r) was used to derive the line, which is shown with 95% confidence limits (dashed lines). N=73, 69, and 43 (from left). **(B)** Quantification of EMCs executed by *itr-1/acd-5* single and double mutants. Significance was assessed by a Kruskal-Wallis test with Dunn's multiple comparison test (wt vs. *itr-1* mutant *p=0.00245; wt vs. *acd-5(ok2657)/itr-1* mutant ***p=0.0005; *acd-5(ok2657)* vs. *itr-1* mutant *p=0.0307; *acd-5(ok2657)* vs. *acd-5(ok2657)/itr-1* mutant ***p=0.0008). **(C)** Quantification of pBocs executed by *itr-1/acd-5* single and double mutants. The Kruskal-Wallis test was non-significant (p=0.11). For **(B, C)**, error bars represent mean and SEM, 15<N<26. **(D)** Quantification of EMCs executed by *pbo-4* and *acd-5* single and double mutants. Significance was assessed by a Kruskal-Wallis test with Dunn's multiple comparison test (*p=0.0456). Neither double mutant was different from *pbo-4(ok538)* (p=1). Error bars represent mean and SEM. **(E)** Coefficient of variation of cycle length for *pbo-4* and *acd-5* single and double mutants. The Kruskal-Wallis test was non-significant (p=0.459). Error bars represent median and IQR. **(F)** Quantification of pBoc strength of *pbo-4* and *acd-5* single and double mutants. *p=0.232, ***p=0.0003, ns p=3.077, Fisher exact test. For clarity, non-significant results are omitted from graphs **(B–E)**. For **(D–F)**, N=12 for wild-type, 8 for all other strains, from 5 cycles/6 events per animal.

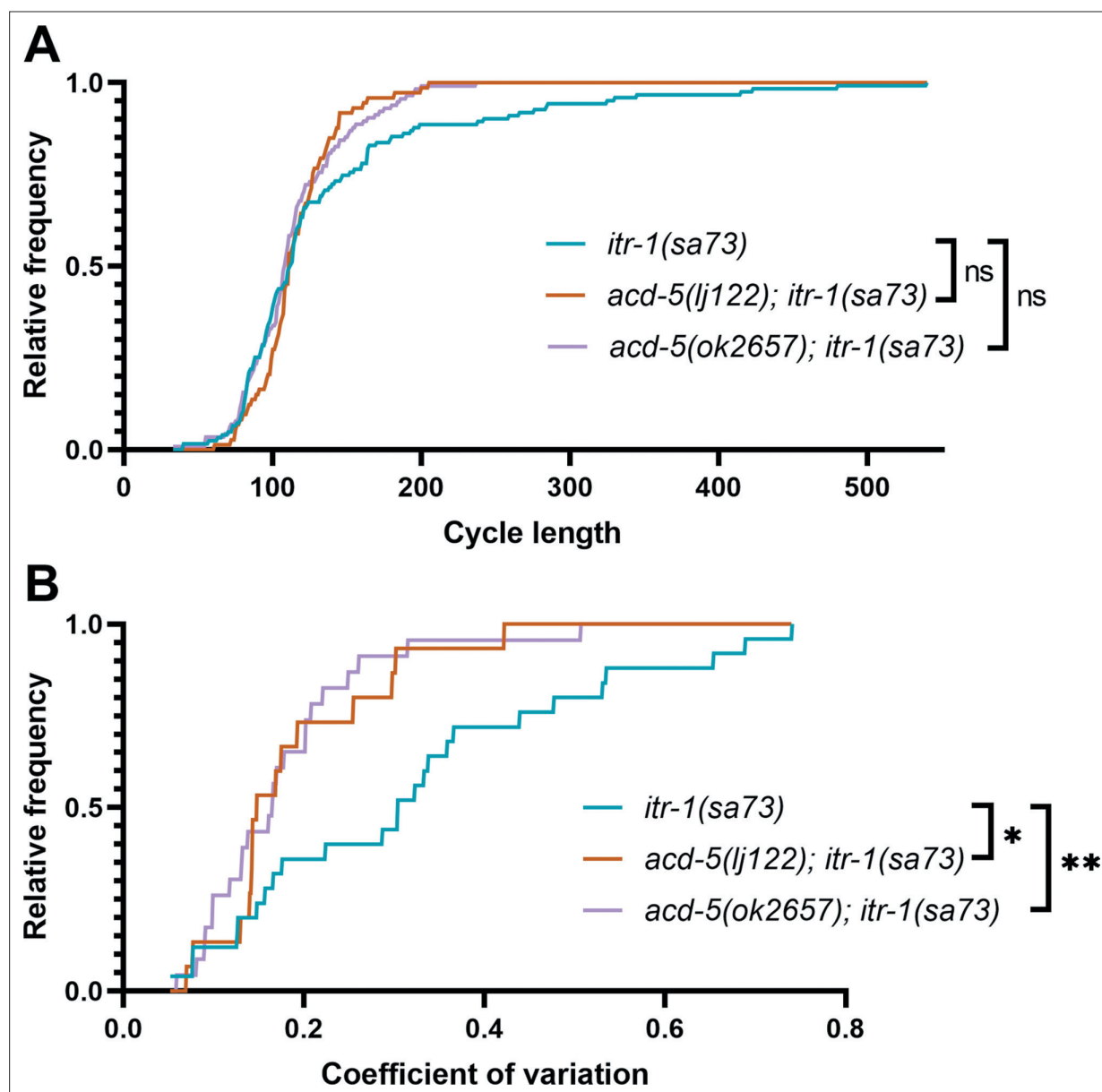


Figure 3—figure supplement 4. Comparison of cumulative distribution of cycle length and coefficient of variation in *itr-1(sa73)* strains. Cumulative distributions using the data from **Figure 3E**. **(A)** DMP cycle length. Distribution of cycle length was compared using a Kolmogorov-Smirnov for complimentary cumulative distribution. *itr-1(sa73)* was not significantly different from *acd-5(ok2657); itr-1(sa73)* ($p=0.3322$, ns, $D=0.123$) or *acd-5(lj122); itr-1(sa73)* ($p=0.0837$, ns, $D=0.186$). **(B)** Coefficient of variation of cycle length. *itr-1(sa73)* was significantly different from both *acd-5(ok2657); itr-1(sa73)* (** $p=0.0037$, $D=0.513$) and *acd-5(lj122); itr-1(sa73)* (* $p=0.021$, $D=0.493$).

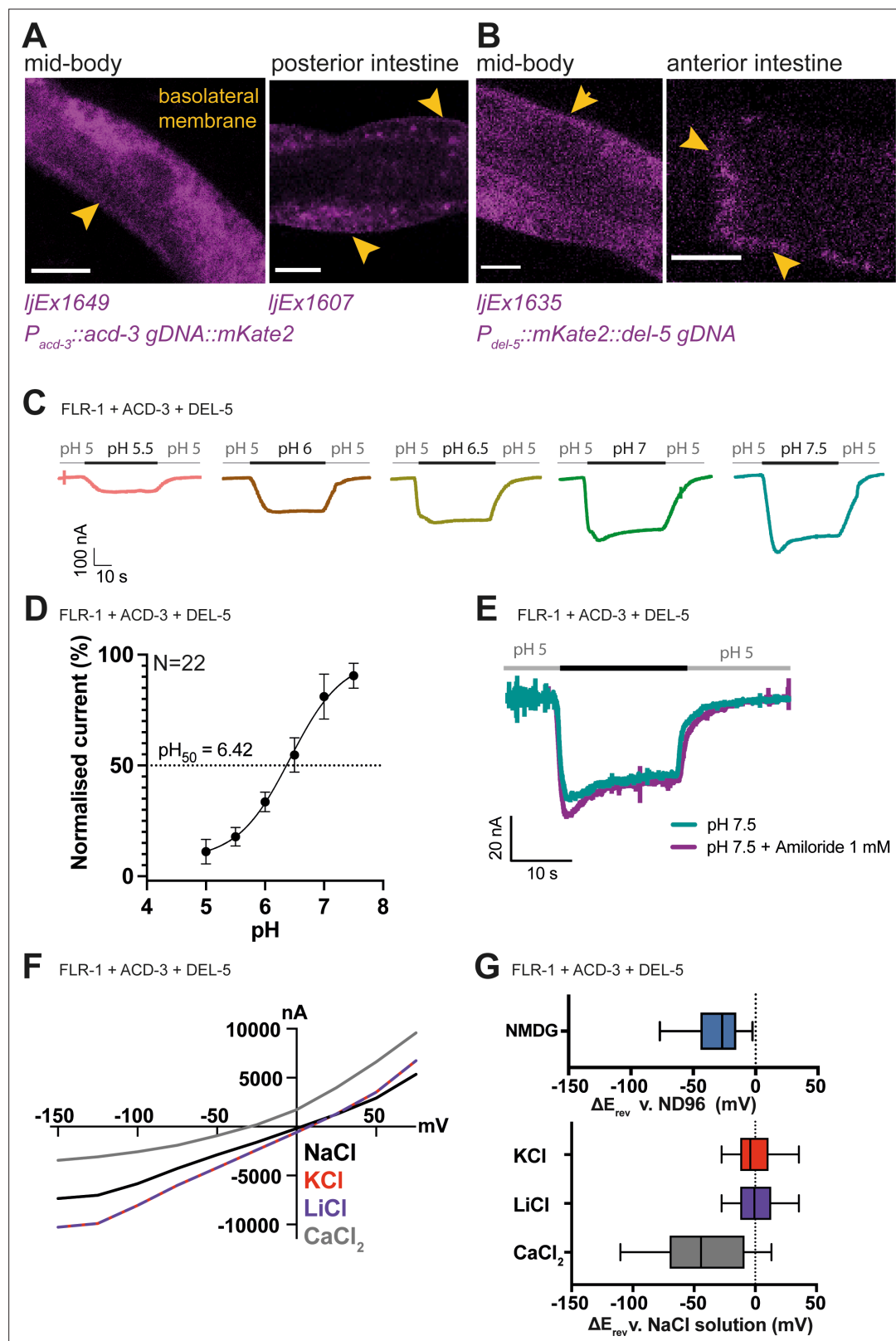


Figure 4. FLR-1 can form pH-sensitive heteromeric channels with ACD-3 and DEL-5. **(A)** ACD-3 is localised at the basolateral intestinal membrane. Localisation of mKate2-C-terminally tagged ACD-3 *lJEx1649* and *lJEx1607* (*P_{acd-3}::acd-3 gDNA::mKate2*) (magenta) shows evidence of basolateral membrane localisation (yellow arrows). Shown are the mid-body (Left) and the posterior intestine (Right). Scale bar: 10 μ m. **(B)** DEL-5 is localised at the basolateral intestinal membrane. Localisation of mKate2-N-terminally tagged DEL-5 *lJEx1635* (*P_{del-5}::mKate2::del-5 gDNA*) (magenta) shows evidence

Figure 4 continued on next page

Figure 4 continued

of basolateral and lateral membrane localisation (yellow arrows). Shown are the mid-body (Left) and the anterior intestine (Right). Scale bar: 10 μ m. See **Figure 5—figure supplement 3** for evidence that the fusions used in (A) and (B) rescue the defecation phenotypes of *acd-3/del-5* double mutants discussed later. (C) Representative traces from *Xenopus* oocytes injected with *flr-1*, *acd-3*, and *del-5* cRNA (250ng/ μ l of each construct) for the pH ranges pH 5.5–7.5 (gray bar represents perfusion time) from a holding pH of 5. Currents were recorded at a holding potential of –60mV and traces are baseline-subtracted and drift-corrected using the Roboocyte²⁺ (Multichannels) software. (D) pH response curve (I/I_{\max} as percentage) covering the ranges pH 5–7.5 from a holding pH of pH 5. N=22. Mean \pm SEM. Currents were recorded at a holding potential of –60mV, normalised to maximal currents and best fitted with the Hill's equation (Nonlin fit Log(inhibitor) versus normalised response–variable slope) in GraphPad Prism. (E) The FLR-1/ACD-3/DEL-5 heteromeric channel is insensitive to the blocker amiloride. Representative traces from *Xenopus* oocytes injected with *flr-1*, *acd-3*, and *del-5* cRNA (250ng/ μ l of each construct) perfused with pH 7.4 (black line) in the absence (cyan) or in the presence (purple) of 1mM amiloride. Currents were recorded at a holding potential of –60mV. (F) Current-voltage (I-V) curve representative trace and (G) change in reversal potential (median and IQR, Tukey method), ΔE_{rev} when shifting from a ND96 to NMDG solution (top) (N=14 oocytes) or from a NaCl solution to KCl, LiCl, or CaCl₂ solution (bottom) (N=16 oocytes).

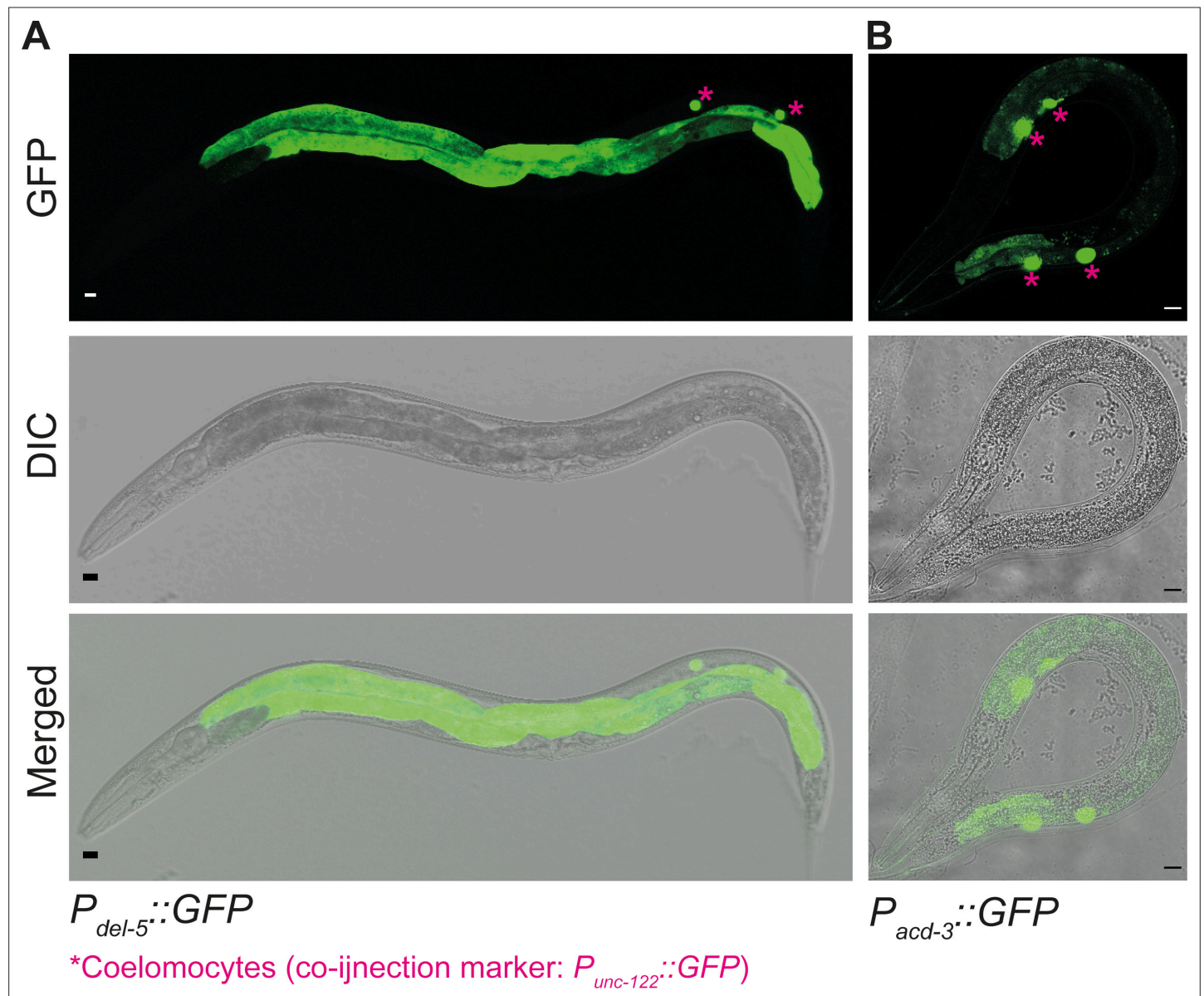


Figure 4—figure supplement 1. *acd-3* and *del-5* are expressed in the intestine. Transcriptional reporters of (A) *del-5* (lJEx1349) and (B) *acd-3* (lJEx1345) expression, using the 5' promoter sequences fused to the GFP gene. Scale bars are 10 μ m.

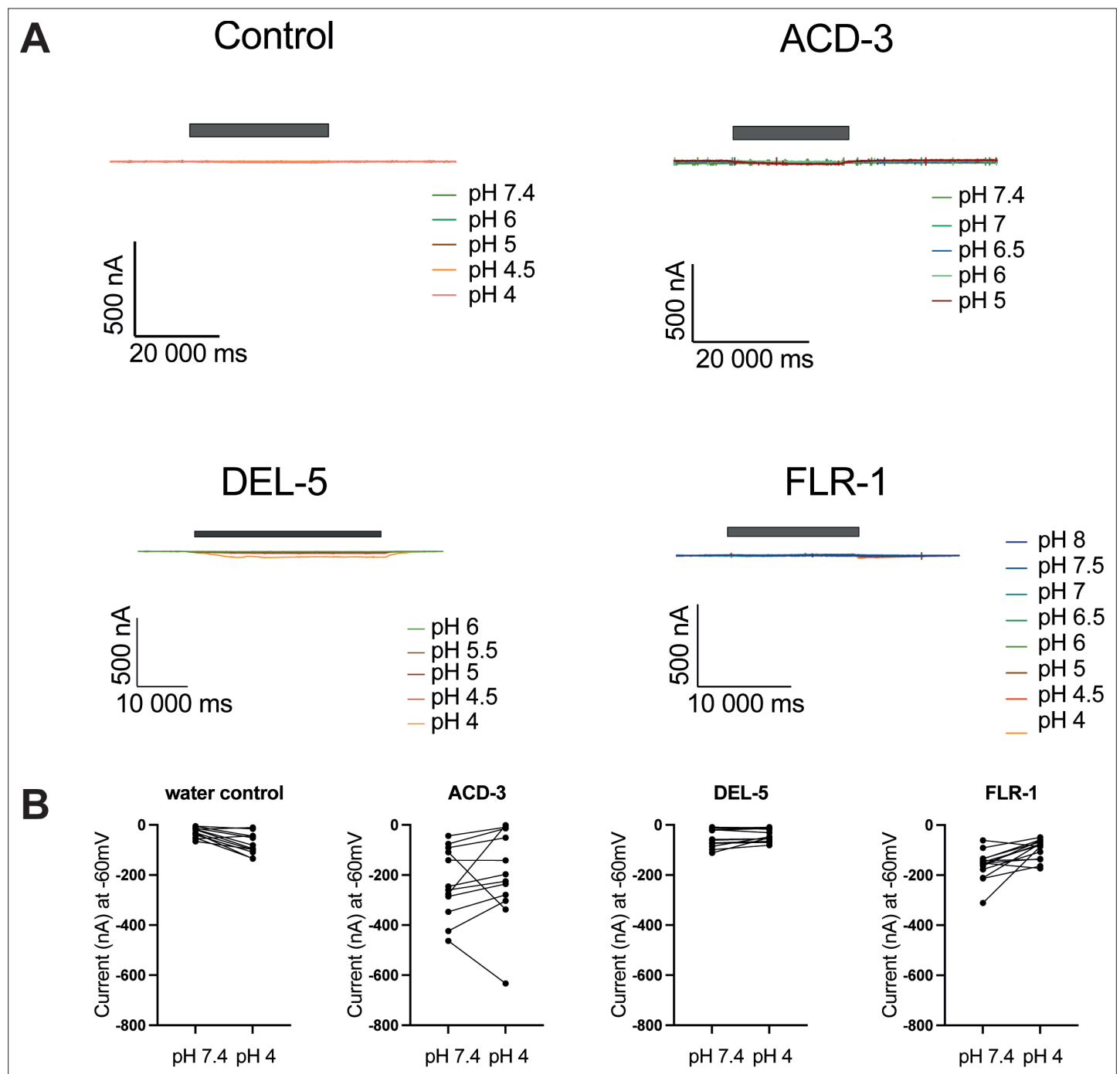


Figure 4—figure supplement 2. Characterisation of ACD-3, DEL-5, and FLR-1 homomeric channel acid-sensing properties. **(A)** Representative traces of *Xenopus* oocytes injected with *acd-3*, *del-5*, or *flr-1* cRNA (500 ng/μl) or water. Currents were recorded at a holding potential of -60 mV and traces are baseline-subtracted and drift-corrected using the Roboocyte²⁺ (Multichannels) software. **(B)** Actual currents of *Xenopus* oocytes injected with nuclease-free water (control), *acd-3*, *del-5*, or *flr-1* cRNA when perfused with pH 7.4 versus pH 4 (each individual oocyte is connected by a line). N=8, 13, 14, and 6, respectively. For ease of visualisation, inward currents are converted to positive values.

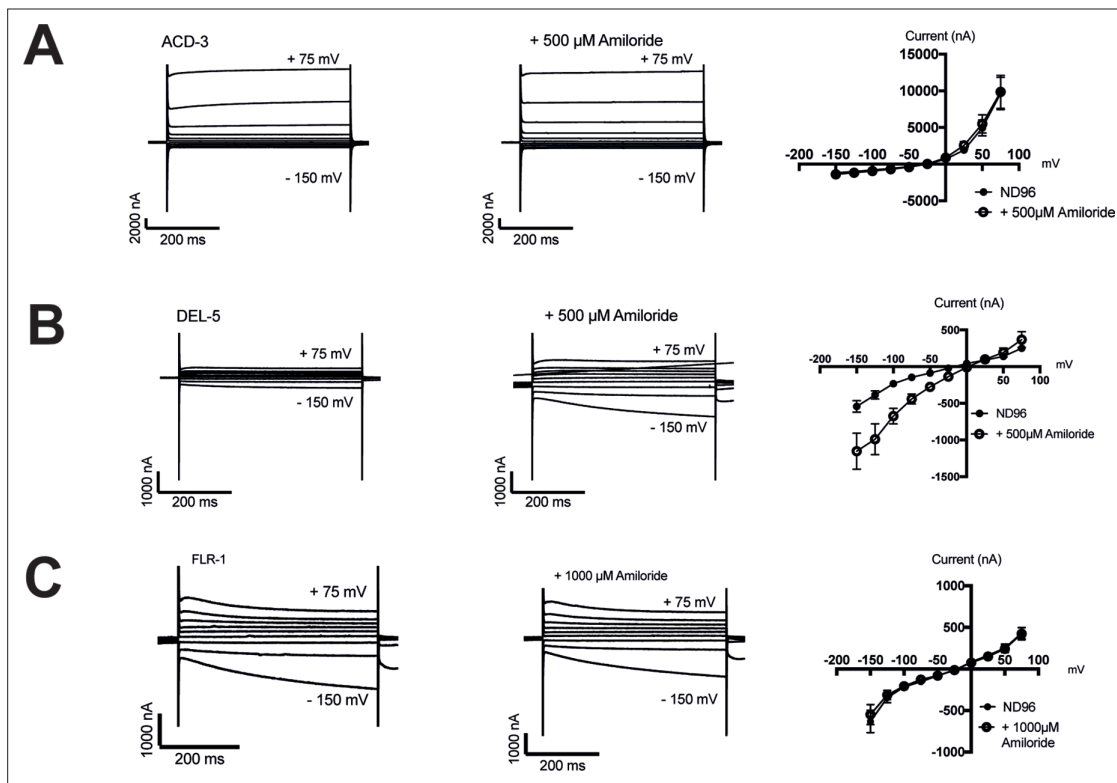


Figure 4—figure supplement 3. Characterisation of ACD-3, DEL-5, and FLR-1 homomeric channel amiloride-sensitivity. (A–C) Representative traces and current-voltage relationships when *Xenopus* oocytes injected with *acd-3*, *del-5*, or *flr-1* cRNA were perfused with a neutral solution (ND96, pH 7.4) in the presence and absence of 500 μ M or 1000 μ M amiloride. N=5, 6, and 8, respectively. Error bars represent mean and SEM.

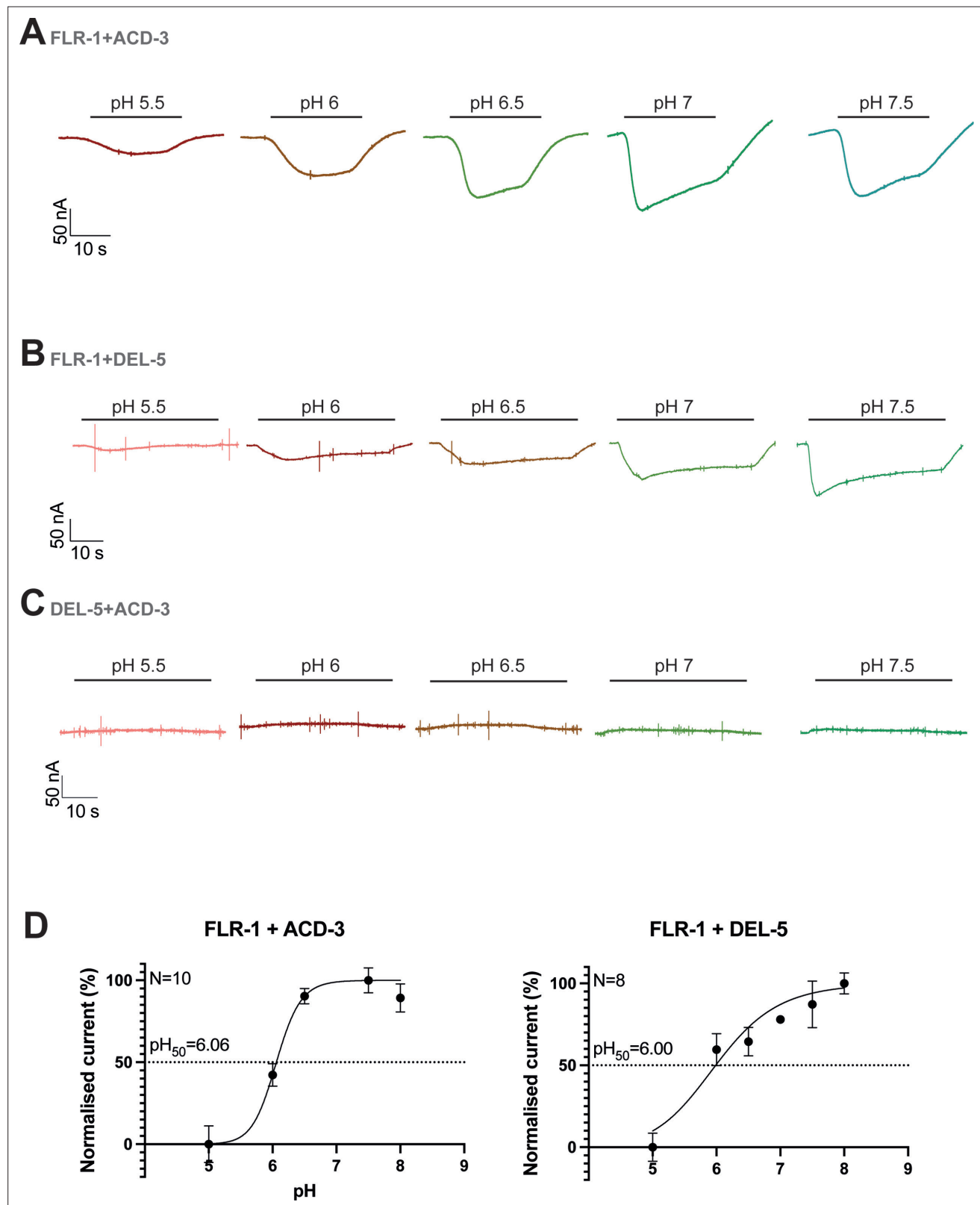


Figure 4—figure supplement 4. FLR-1 can form a pH-sensitive channel with ACD-3 or DEL-5. (A–C) Representative traces of *Xenopus* oocytes injected with *flr-1* cRNA with *acd-3* or *del-5* cRNA or *acd-3* and *del-5* cRNA (250 ng/μl for each construct). Black bar represents time of perfusion with the indicated pH. (D) pH response curve (I/I_{\max} expressed as percentage) covering the ranges pH 5–8 from a holding pH of 5. N is the number of oocytes. Mean \pm SEM. Currents were recorded at a holding potential of -60 mV, normalized to maximal currents and best fitted with the Hill equation (Nonlin

Figure 4—figure supplement 4 continued on next page

Figure 4—figure supplement 4 continued

fit Log(inhibitor) vs. normalised response–variable slope) in GraphPad Prism. Traces are baseline-subtracted and drift-corrected using the Roboocyte²⁺ (Multichannels) software.

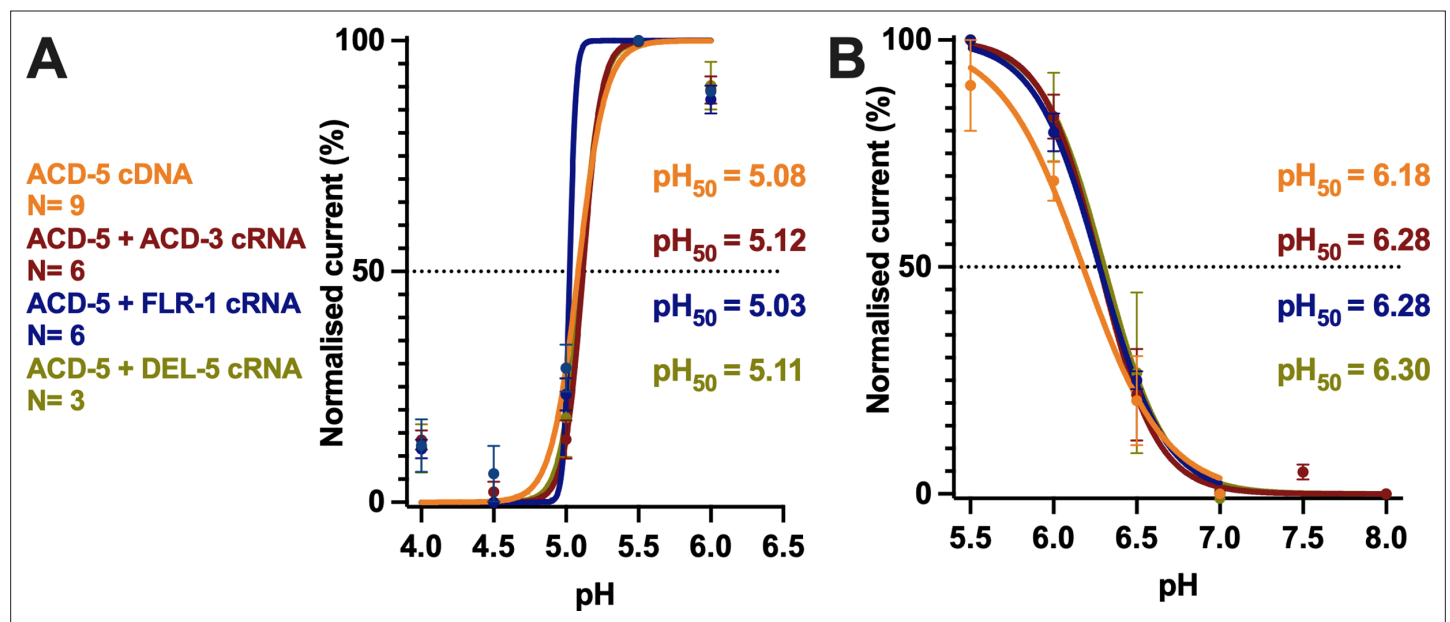


Figure 4—figure supplement 5. Co-expression with FLR-1, ACD-3, or DEL-5 does not change the pH_{50} of ACD-5. PH response curve (I/I_{max} as percentage) covering the ranges (A) pH 4–6 and (B) pH 5.5–8 from a holding pH of 7.4. pH_{50} for each construct is indicated in the respective colour. N is the number of oocytes. Mean \pm SEM. Currents were recorded at a holding potential of -60 mV, normalised to maximal currents and best fitted with the Hill equation (Nonlin fit Log(inhibitor) vs. normalised response–variable slope) in GraphPad Prism.

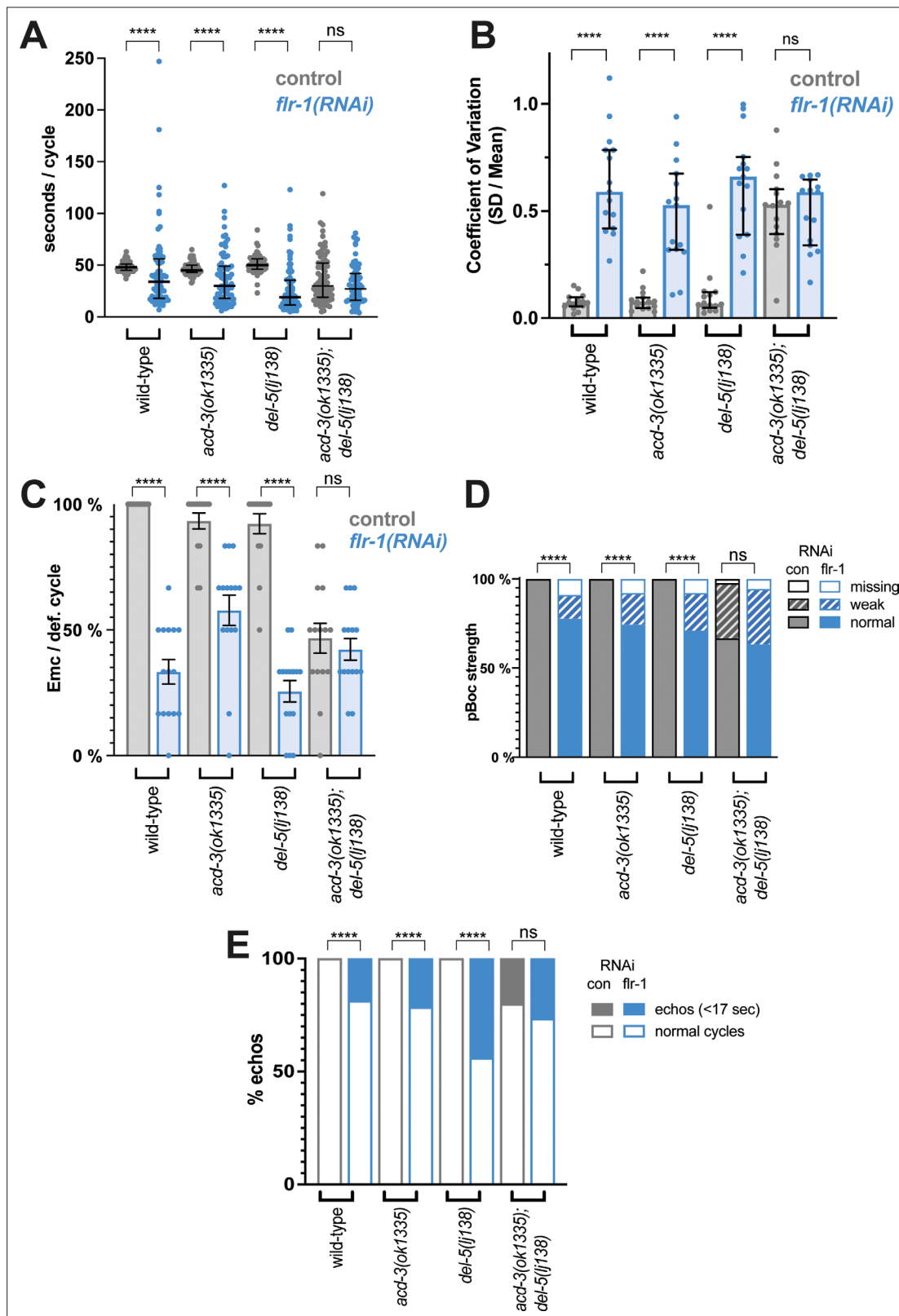


Figure 5. Knockdown of *flr-1* and mutations in *acd-3/del-5* results in arrhythmic DMP intervals, missed muscle contractions, and echos. FLR-1 or ACD-3/DEL-5 depletion alters cycle length and variability. (A) DMP interval and (B) coefficient of variation of animals on *flr-1(RNAi)* (blue) versus control RNAi (grey) assessed by a Mann-Whitney U-test (**** $p < 0.0001$, *acd-3(ok1335)*; *del-5(lj138)* control vs. *flr-1(RNAi)* $p = 0.0892$ for cycle length, $p = 0.5$ for CV). Error bars represent median and IQR. (C) Percentage of missed EMCs (mean and SEM) (**** $p < 0.0001$; *acd-3(ok1335)*; *del-5(lj138)* control vs. *flr-1(RNAi)*).

Figure 5 continued on next page

Figure 5 continued

p=0.2535, Mann-Whitney). **(D)** Percentage of cycles displaying the pBoc characteristics indicated (****p<0.0001; *acd-3(ok1335); del-5(lj138)* control vs. *flr-1 (RNAi)* p=0.5861, Fisher exact test). **(E)** Percentage of 'echo' cycles, defined as cycles that last for under 17s (**Teramoto and Iwasaki, 2006; Liu and Thomas, 1994**) (****p<0.0001; *acd-3(ok1335); del-5(lj138)* control vs. *flr-1 (RNAi)* p=0.4516, Fisher exact test). N=13–15 animals for each genotype × 5 cycles scored for each animal.

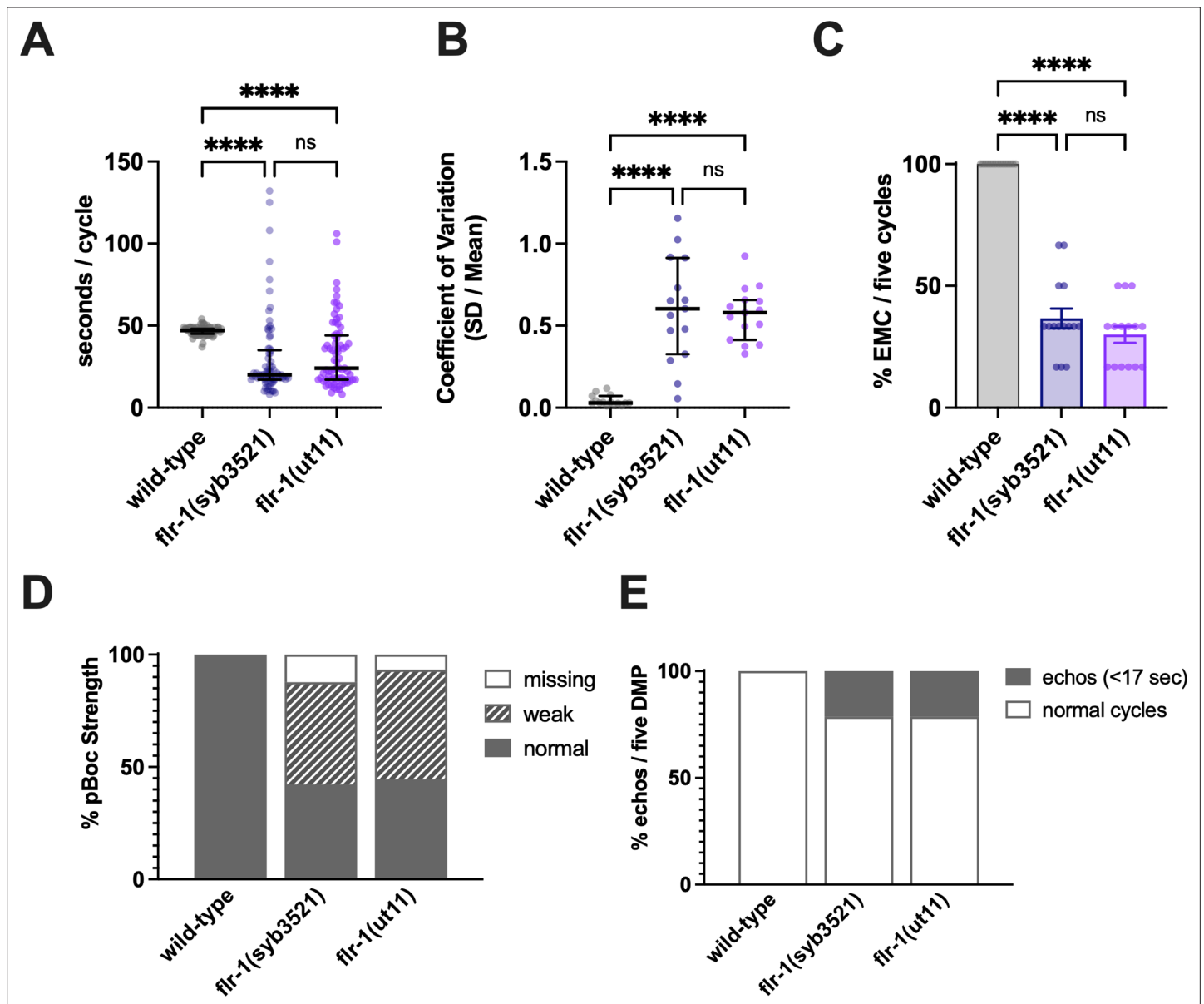


Figure 5—figure supplement 1. *flr-1(ut11)* and *flr-1(syb3521)* mutants show similar phenotypes. Comparison of *flr-1(ut11)* and *flr-1(syb3521)* reveals similar defecation defects: Increased variability of cycle length, with a mix of very short and long cycles; missed EMCs and missed or weak pBocs. **(A)** Cycle length (median and IQR). Significance was assessed by a Kruskal-Wallis test with Dunn's multiple comparison test (**** $p < 0.0001$, $p = 0.7514$, ns). **(B)** Coefficient of variation (CV; median and IQR). Significance was assessed by a Kruskal-Wallis test with Dunn's multiple comparison test (**** $p < 0.0001$, $p > 0.9999$, ns). **(C)** Percentage of missed EMCs (mean and SEM). Significance was assessed by a Kruskal-Wallis test with Dunn's multiple comparison test (**** $p < 0.0001$, $p > 0.9999$, ns). **(D)** Percentage of pBocs displaying the characteristics indicated. **(E)** Percentage of echo cycles. $N = 15$ animals, five cycles scored for each animal.

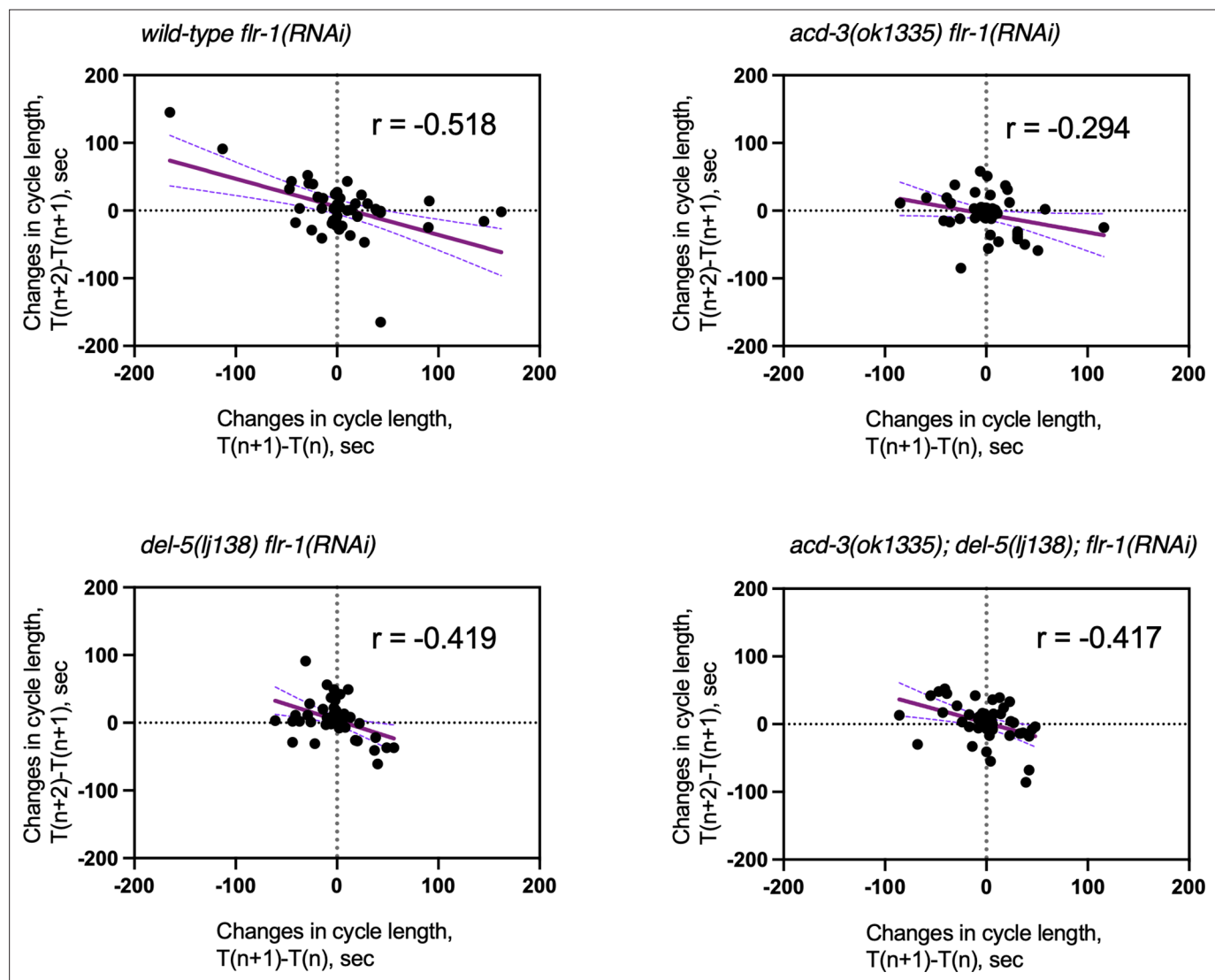


Figure 5—figure supplement 2. Analysis of the defecation cycle of single and double mutants on *flr-1(RNAi)* reveals compensatory behaviour in the oscillator. Scatter plot of the change in period time in one cycle pair compared to the subsequent cycle pair for mutants on *flr-1(RNAi)*. $T(n)$ is the period of the cycle n . Linear regression (Person's r) was used to derive the line which, is shown with 95% confidence limits (dashed lines). $N=13-15$ for each genotype, five cycles scored for each animal.

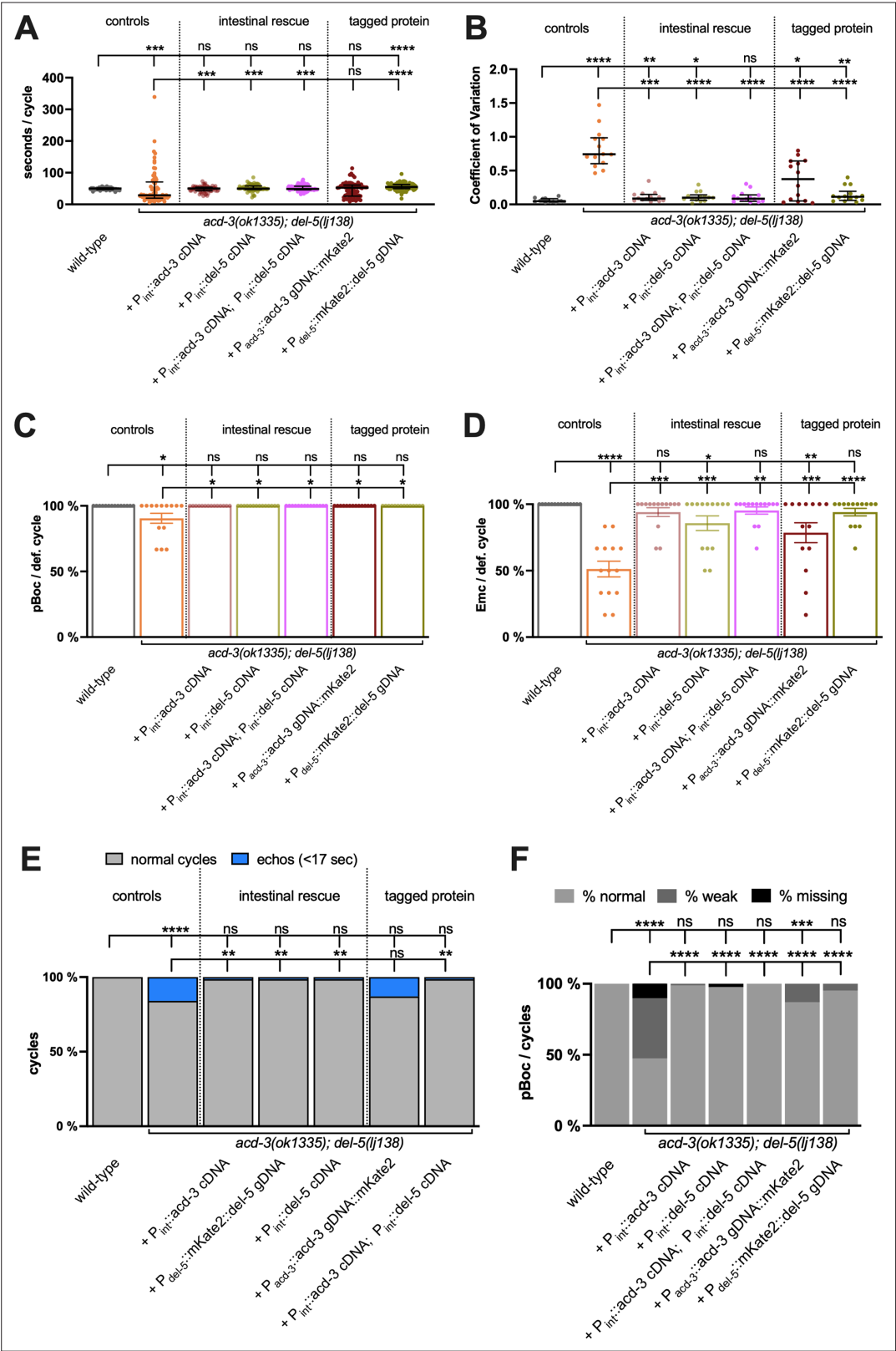


Figure 5—figure supplement 3. Intestine-specific expression of *acd-3* or *del-5*, or expression of *acd-3* or *del-5* fluorophore fusions, rescues DMP defects of *acd-3/del-5* double mutants. (A) Quantification of DMP interval length and (B) coefficient of variation for *acd-3(ok1335); del-5(lj138)* double mutant animals, rescued with the constructs indicated. Error bars represent median and IQR. (C) Expression of *acd-3* or *del-5* can rescue the missed pBoc

Figure 5—figure supplement 3 continued on next page

Figure 5—figure supplement 3 continued

muscle contractions, (D) missed EMCs (mean and SEM), (E) 'echo' DMPs (defined as cycles that last for under 17 s) and (F) strength of pBoc, as percentages of five cycles for each of the 15 individual animals scored. Intestinal specific rescues of either *acd-3* or *del-5* *lJEx1634* [*P_{int}::acd-3 cDNA*] and *lJEx1637* [*P_{int}::del-5 cDNA*] or both *lJEx1641* [*P_{int}::acd-3 cDNA; P_{int}::del-5 cDNA*] and tagged proteins *lJEx1635* [*P_{del-5}::mKate2::del-5 gDNA*] and *lJEx1640* [*P_{acd-3}::acd-3 gDNA::mKate2*] under their endogenous promoters are able to ameliorate the severe phenotypes of *acd-3/del-5* mutants. All groups are assessed by a Mann-Whitney U-test, see **Table 1** for p values. N=14 animals for each genotype, except *acd-3(ok1335)*, *del-5(lj138)*, 13 animals × 5 cycles scored for each animal.

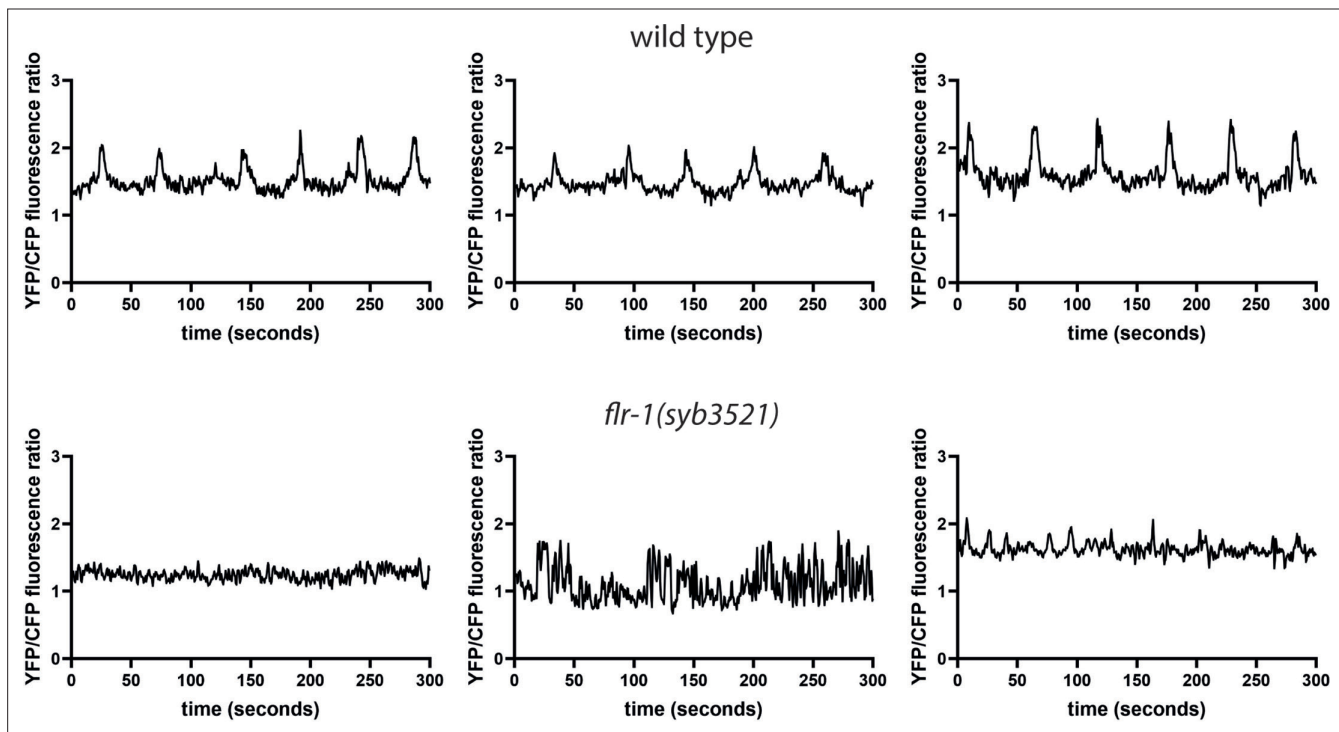


Figure 6. FLR-1 is required for rhythmic intestinal Ca^{2+} transients. Representative example traces of Ca^{2+} transients in the posterior intestinal cells (int9), recorded in freely moving animals expressing the ratiometric indicator D3cpv.

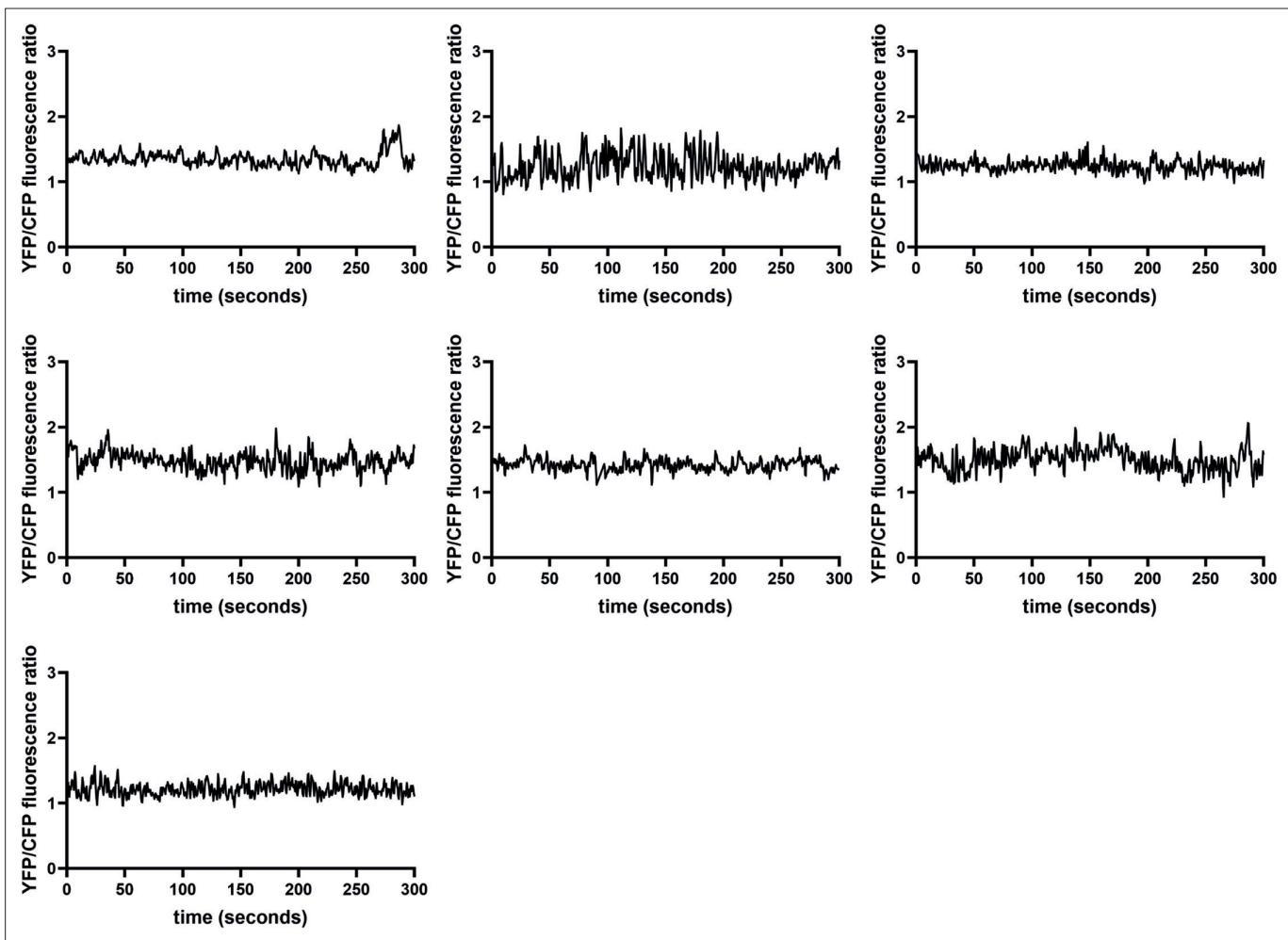


Figure 6—figure supplement 1. Additional intestinal Ca^{2+} traces for *flr-1(syb3521)*, demonstrating the disruption of rhythmicity. Ca^{2+} transients in the posterior intestinal cells (int9), recorded in freely moving animals expressing the ratiometric indicator D3cpv. This supplements the examples shown in **Figure 6**, showing all additional traces used in **Figure 6—figure supplement 3**.

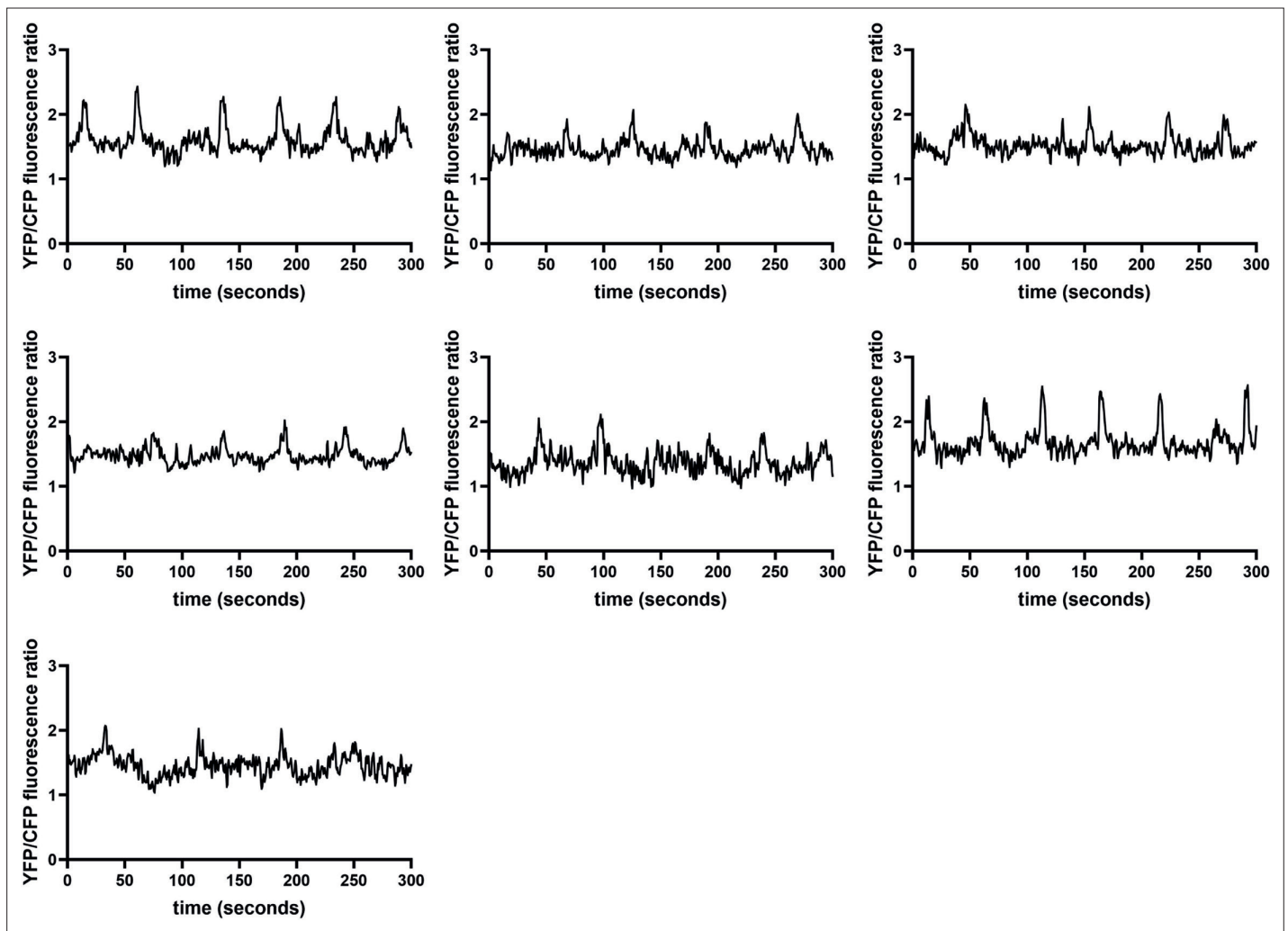


Figure 6—figure supplement 2. Additional intestinal Ca^{2+} traces for wild-type animals, demonstrating the rhythmicity of oscillations. Ca^{2+} transients in the posterior intestinal cells (int9), recorded in freely moving, defecating animals expressing the ratiometric indicator D3cpv. This supplements the examples shown in **Figure 6**, showing all additional traces used in **Figure 6—figure supplement 3**.

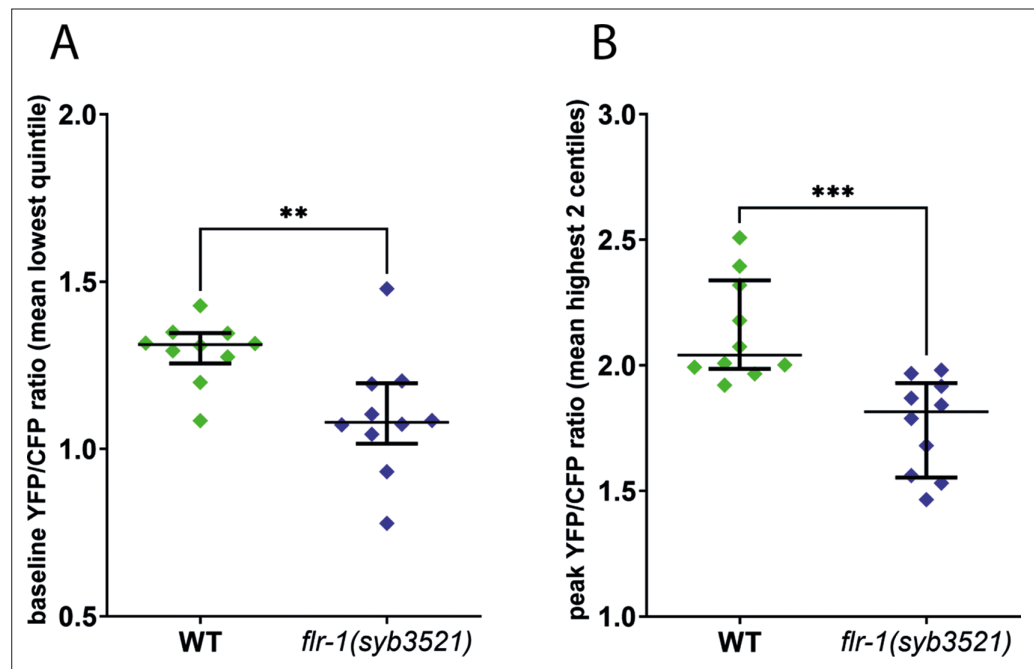


Figure 6—figure supplement 3. FLR-1 is required for rhythmic intestinal Ca^{2+} oscillations. Ca^{2+} imaging of the posterior intestinal (int9) cells of freely moving, defecating animals. **(A)** *flr-1(syb3521)* animals exhibit reduced baseline Ca^{2+} levels. Scatter plot of mean YFP/CFP fluorescence ratio, for the frames corresponding to the lowest quintile, as a measure of baseline ratio, ** $p=0.0076$, unpaired t-test. **(B)** *flr-1(syb3521)* animals exhibit reduced maximal Ca^{2+} levels. Scatter plot of mean YFP/CFP fluorescence ratio, for the frames corresponding to the two highest centiles, as a measure of maximal ratio, *** $p=0.0005$, unpaired t-test. Each data point is the mean for the relevant frames, for an individual recording; error bars are SEM, $N=10$ animals.

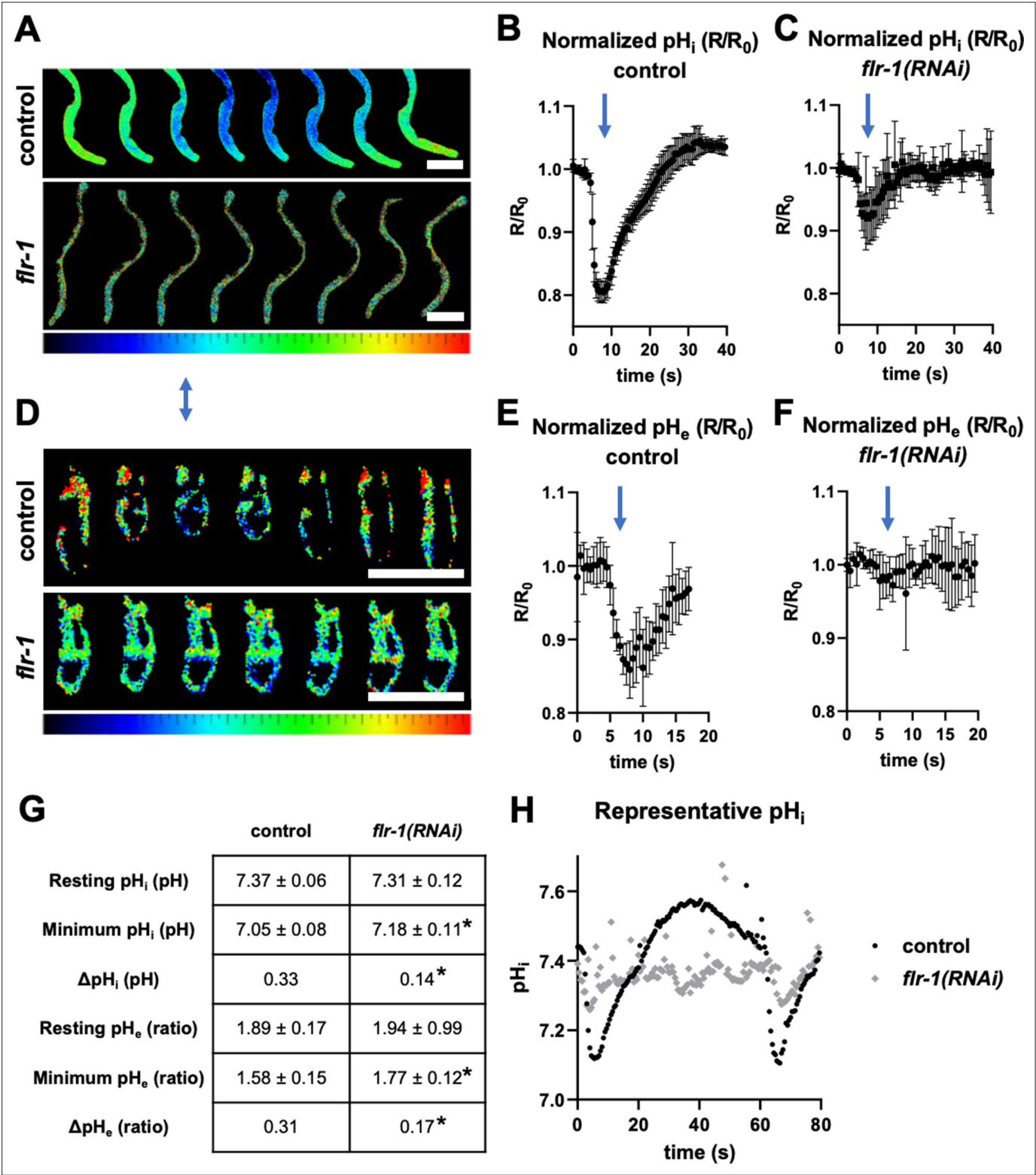


Figure 7. FLR-1 is required for rhythmic intracellular intestinal and pseudocoelomic pH oscillations. Dynamic ratiometric fluorescent imaging to measure pH in freely moving, defecating animals. (A–C) Animals expressing an intestinal cytoplasmic pH-sensitive GFP construct pHluorin, to measure pH_i . (D–F) Animals expressing an extracellular pH biosensor localised to the basolateral membrane of int9, to measure pH_e . (A, D) Composites of adjacent frames extracted from a representative experiment, with relative pH values mapped to a ratio palette, as shown. Images were acquired at 2Hz, and each series is time normalised to pBoc. Animals are oriented anterior upward. Blue arrow denotes pBoc. Scale bars indicate 100 μ m. (B–C) Plots of R/R_0 for pH_i , time-normalised to pBoc, in control and *flr-1(RNAi)* treated worms, as indicated (N=6). (E–F) Plots of R/R_0 for pH_e , time-normalised to pBoc, in control

Figure 7 continued on next page

Figure 7 continued

and *flr-1(RNAi)* treated worms, as indicated (N=6). Note that the x-axis differs for pH_i and pH_e traces. **(G)** Mean pH_i ± SD (calculated using a Boltzmann calibration) or pH_e (ratio) ± SD (raw YFP/CFP ratio, as calibration was not possible for this biosensor) for the resting and minimum observed values, as well as ΔpH (N=6). Control and respective *flr-1(RNAi)* means were statistically compared using two-tailed, unpaired t-tests (*p<0.05). **(H)** Single, extended pH_i traces (80s) to highlight the arrhythmia, weak internal acidification, and 'echo' cycles observed in many *flr-1(RNAi)* animals.

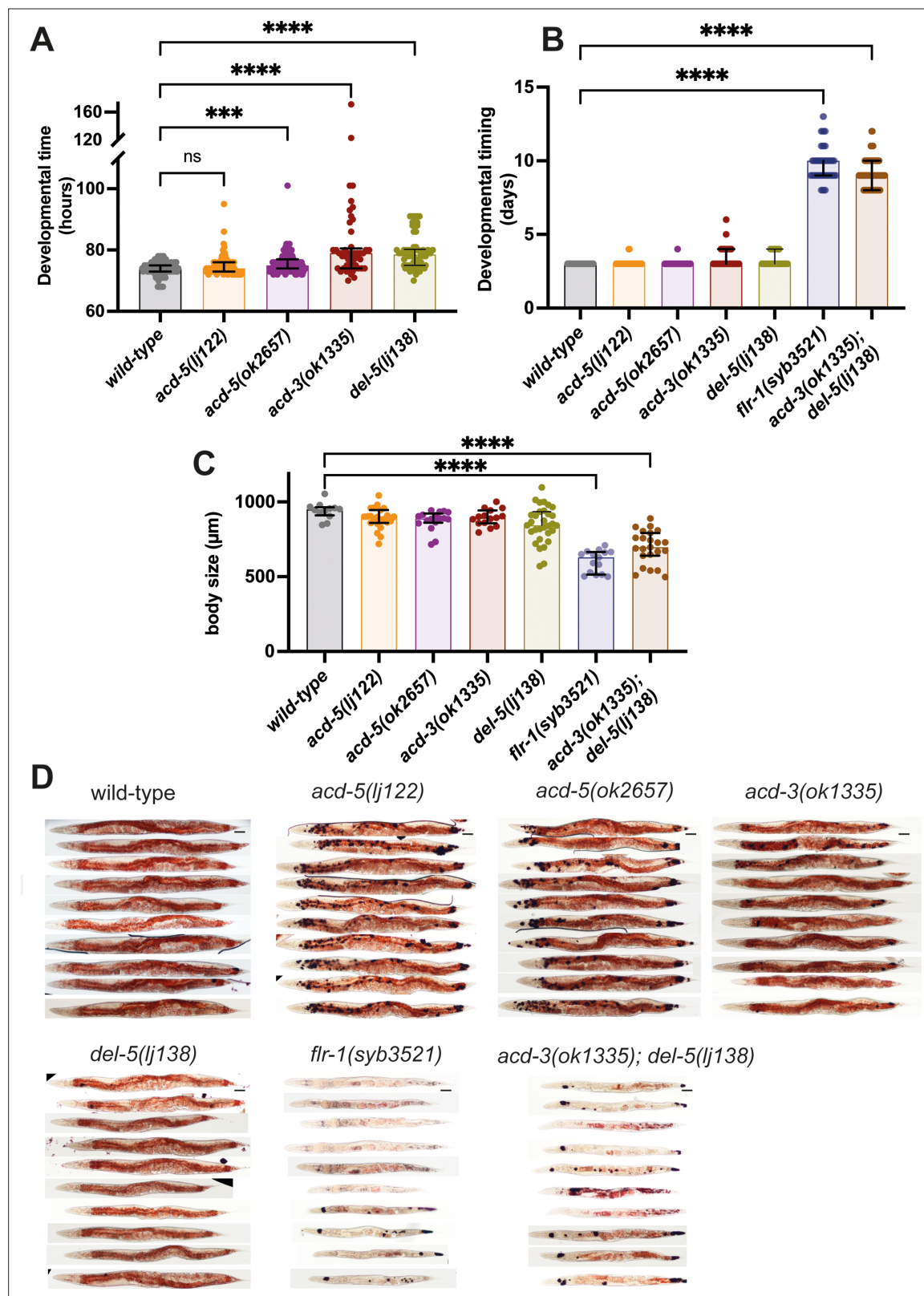


Figure 8. Consequences of disruptions of proton signalling in the intestine. (A) *acd-5(ok2657)*, *acd-3*, and *del-5* single mutants show a subtle developmental delay. Developmental timing (generation time) of DEG/ENaC single mutants in hours from egg laid to first egg laid as an adult. N=115, 102, 96, 49, and 62, in order on graph. Kruskal-Wallis test with Dunn's multiple comparison post hoc test, *** $p=0.0004$, **** $p<0.0001$. (B) *flr-1* single mutants and *acd-3/del-5* double mutants show a severe developmental delay. Developmental timing of DEG/ENaC single, double and triple mutants in

Figure 8 continued on next page

Figure 8 continued

days from egg-laid to day of onset of egg-laying. N=as in (A) for single mutants; 76, 92 for the remainder. (C) *flr-1* single mutants and *acd-3/del-5* double mutants are short. Quantification of body size of DEG/ENaC single, and double mutants. Each circle is an individual worm. N=12, 23, 17, 15, 31, and 15. Kruskal-Wallis test with Dunn's multiple comparison post hoc test, **** $p < 0.0001$. Error bars indicate median and IQR. Each individual point is one animal. (D) *flr-1* single mutants and *acd-3/del-5* double mutants show aberrant fat metabolism. Fat storage and distribution of DEG/ENaC single and double mutants assessed by Oil-Red-O staining of 10 representative animals. Scale bar: 50 μ m.

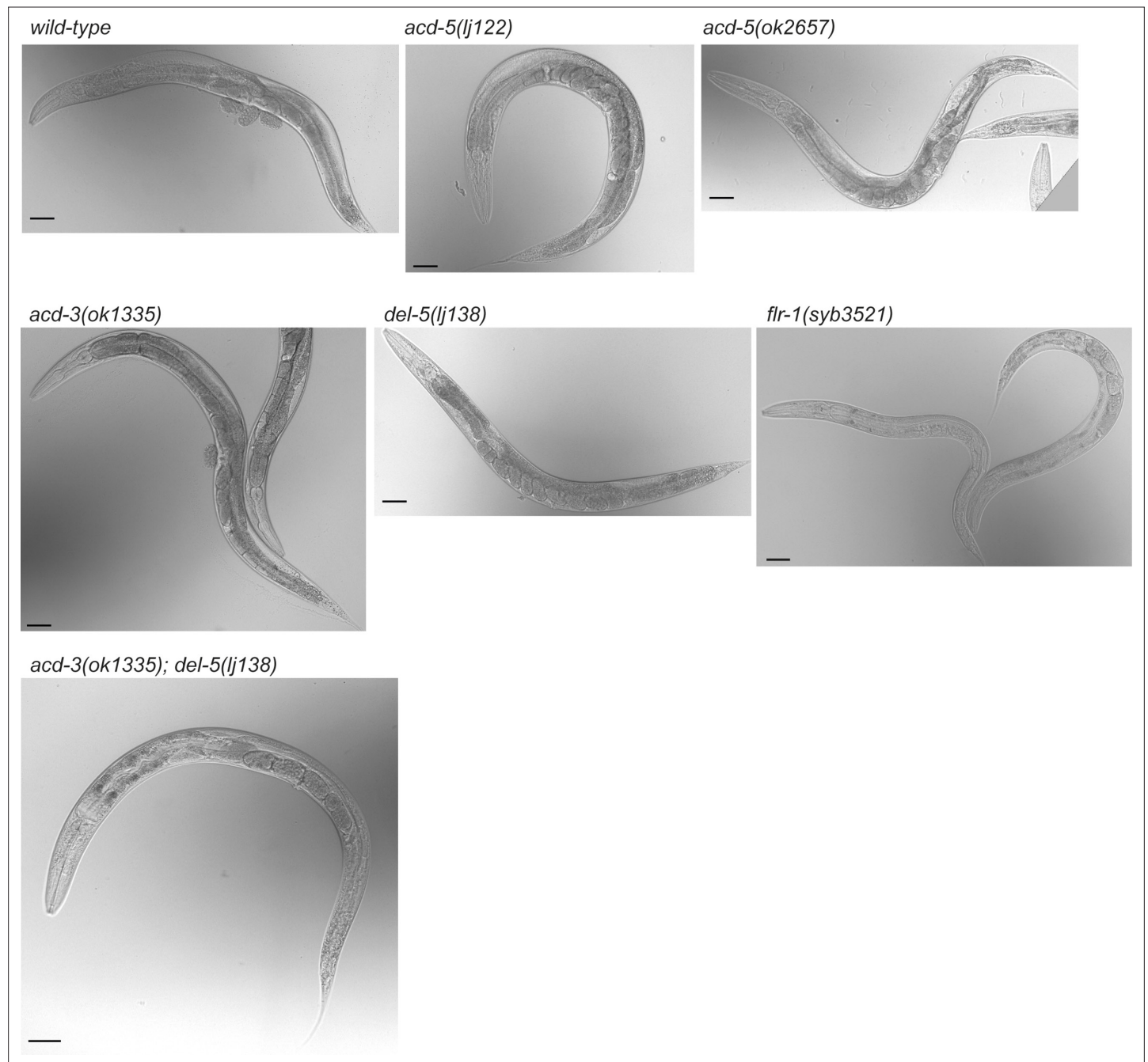


Figure 8—figure supplement 1. *flr-1* and *acd-3/del-5* deficient animals exhibit a caloric restriction phenotype. Single and double mutant day-1 adults for the DEG/ENaCs expressed in the intestine. Single mutants for *acd-5*, *acd-3*, or *del-5* show a wild-type body shape, while *flr-1* single or *acd-3/del-5* double mutants are thin with few eggs. Scale bars are 50 μ m.

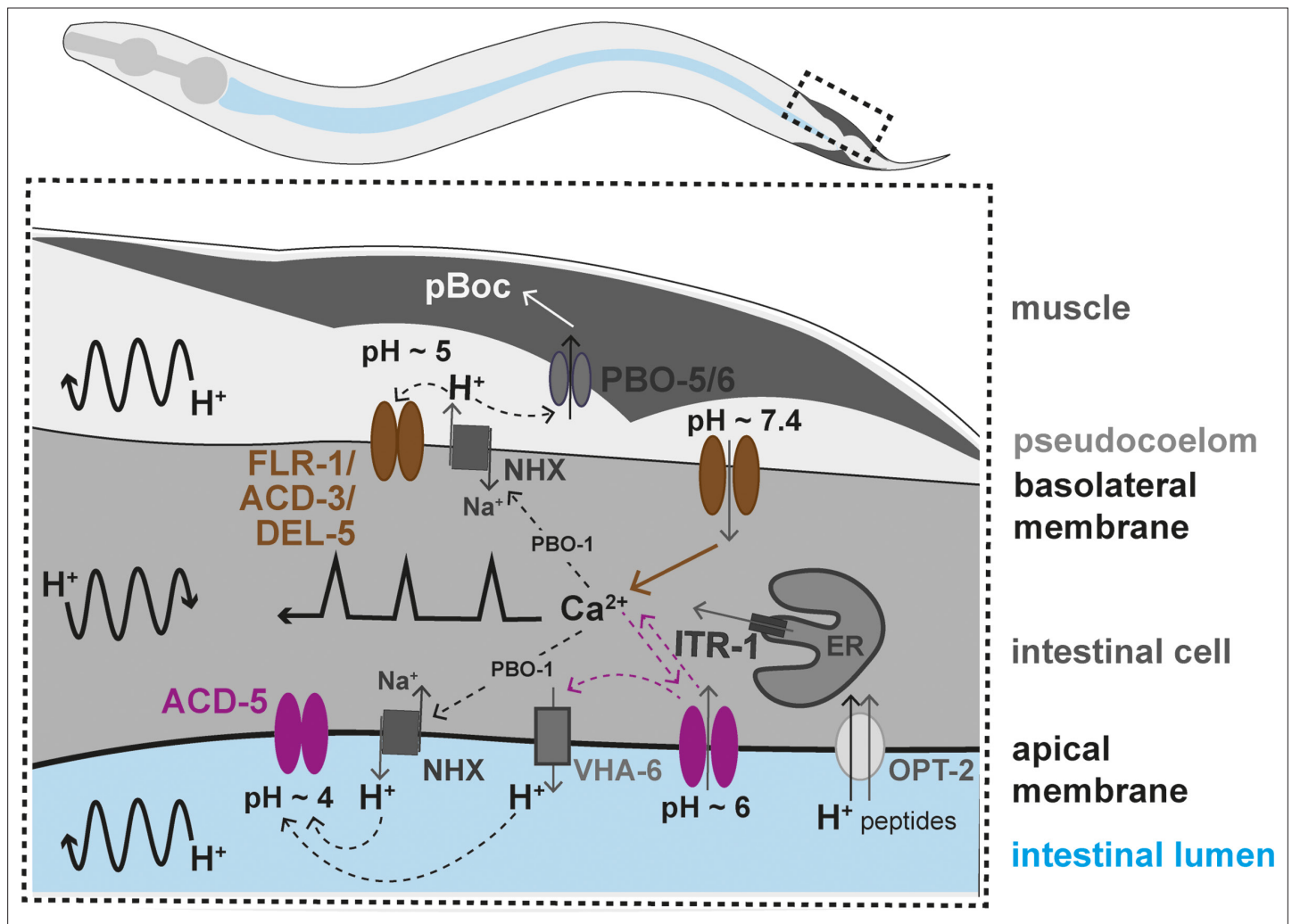


Figure 9. Working model of the two acid-sensing DEG/ENaCs in the *Caenorhabditis elegans* intestinal cells. Ca^{2+} release from the endoplasmic reticulum (ER), via the IP_3 receptor, ITR-1 , is responsible for the Ca^{2+} oscillations transitioning from the posterior to the anterior part of the intestine (represented by the black line with sharp peaks). Ca^{2+} also influences the activity Na^+/H^+ exchangers (NHX) via the CHP1 homolog PBO-1 . H^+ oscillations occur in the intestinal cell, transitioning posteriorly, and pseudocoelom and intestinal lumen, transitioning anteriorly (represented by the curved black arrow lines). The FLR-1/ACD-3/DEL-5 containing channel localises to the basolateral intestinal membrane, it is likely open for much of the cycle, directly affecting Ca^{2+} oscillations and ion homeostasis. The Ca^{2+} transient triggers efflux of H^+ via NHX s (including PBO-4), decreasing pseudocoelomic pH and closing FLR-1/ACD-3/DEL-5 , and Ca^{2+} concentration returns to baseline. ACD-5 is localised at the apical membrane. Proton pumps such as NHX s and VHA-6 maintain the acidity in the lumen during most of the DMP ($\text{pH} \sim 4$, ACD-5 is closed). Once a cycle, H^+ influx, through the $\text{H}^+/\text{dipeptide}$ symporter OPT-2 and other unknown channels raises the luminal pH to about $\text{pH} \sim 6$ (ACD-5 opens), the resulting cation-influx reactivates H^+ efflux (via VHA-6 ?). ACD-5 has limited influence on the Ca^{2+} oscillations, masked by the dominant role of IP_3 signalling.